# RESEARCH ARTICLE

**Key Points:**
- Melt-PX predicts the melting behavior of pyroxenites as a function of $P$, $T$, and $X$
- At $P > {\sim}3.5$ GPa, a large fraction ($>20\%$) of natural pyroxenites have near-solidus temperatures greater than those of fertile peridotite
- Crustal thickness depends on the mass fraction and composition of pyroxenite in the mantle as well as mantle potential temperature

**Supporting Information:**
- Supporting Information S1
- Table S1
- Melt-PX spreadsheet

**Correspondence to:**
S. Lambart,
sarahlambart@yahoo.fr

# The role of pyroxenite in basalt genesis: Melt-PX, a melting parameterization for mantle pyroxenites between 0.9 and 5 GPa

**Sarah Lambart[1,2], Michael B. Baker[1], and Edward M. Stolper[1]**

[1]Division of Geological and Planetary Sciences, California Institute of Technology, Pasadena, California, USA, [2]Department of Earth and Planetary Sciences, University of California, Davis, California, USA

**Abstract** Geochemical and isotopic data suggest that the source regions of oceanic basalts may contain pyroxenite in addition to peridotite. In order to incorporate the wide range of compositions and melting behaviors of pyroxenites into mantle melting models, we have developed a new parameterization, Melt-PX, which predicts near-solidus temperatures and extents of melting as a function of temperature and pressure for mantle pyroxenites. We used 183 high-pressure experiments (25 compositions; 0.9–5 GPa; 1150–1675°C) to constrain a model of melt fraction versus temperature from 5% melting up to the disappearance of clinopyroxene for pyroxenites as a function of pressure, temperature, and bulk composition. When applied to the global set of experimental data, our model reproduces the experimental $F$ values with a standard error of estimate of 13% absolute; temperatures at which the pyroxenite is 5% molten are reproduced with a standard error of estimate of 30°C over a temperature range of ~500°C and a pressure range of ~4 GPa. In conjunction with parameterizations of peridotite melting, Melt-PX can be used to model the partial melting of multilithologic mantle sources—including the effects of varying the composition and the modal proportion of pyroxenite in such source regions. Examples of such applications include calculations of isentropic decompression melting of a mixed peridotite + pyroxenite mantle; these show that although the potential temperature of the upwelling mantle plays an important role in defining the extent of magma production, the composition and mass fraction of the pyroxenite also exert strong controls.

## 1. Introduction

Melting of mantle sources with multiple lithologies, each with its own melting behavior and chemical and isotopic composition, is believed to be an important factor in producing the range of magma compositions observed in individual igneous provinces [*Hofmann*, 2007; *Kogiso et al.*, 2004a; *Lambart et al.*, 2013, and references therein]. The notion that pyroxenites—olivine-poor lithologies dominated by pyroxene under upper mantle conditions—play a significant role in basalt genesis is supported by various geochemical and petrological observations:

1. Although it is widely debated as to when plate tectonics began (see *Arndt* [2013] and *Korenaga* [2013] for reviews), oceanic crust (which converts to pyroxene-rich rocks under mantle conditions) has likely been subducted back into the mantle over the last several gigayears and has been suggested as a reservoir in the mantle for certain incompatible trace elements [e.g., *Hauri and Hart*, 1997; *Kamber and Collerson*, 2000; *McDonough*, 1991; *Rudnick et al.*, 2000; *Sun et al.*, 2011]. Other processes such as lithospheric delamination [e.g., *Elkins-Tanton*, 2005; *Kay and Mahlburg Kay*, 1993; *Lee*, 2014], mantle wedge metasomatism [e.g., *Kelemen et al.*, 1998; *Rapp et al.*, 1999; *Straub et al.*, 2008; *Yaxley and Green*, 1998], and emplacement of magmas and metasomatism in the lithosphere [e.g., *Humphreys and Niu*, 2009; *Niu*, 2008; *Pilet et al.*, 2005, 2008] can also introduce pyroxene-rich lithologies into the mantle.

2. Pyroxenites are ubiquitous in orogenic massifs and ophiolites [*Bodinier and Godard*, 2003] and are also sampled as mantle xenoliths [*Pearson et al.*, 2003]. Based on the proportions of pyroxenites in orogenic massifs, pyroxenites may constitute 2 to 5% of the Earth's upper mantle and can locally reach up to 10% (e.g., in Beni Bousera [*Pearson and Nixon*, 1996]). Such occurrences of pyroxene-rich rocks in the upper mantle inspired the "marble cake model" of *Allègre and Turcotte* [1986].

3. High-pressure melting experiments on pyroxene-rich lithologies [e.g., *Green and Ringwood*, 1967; *Kornprobst*, 1970; *Lambart et al.*, 2009a; *Pertermann and Hirschmann*, 2003a; *Yasuda et al.*, 1994; *Yaxley and Green*, 1998] demonstrate that at the same pressure, many pyroxenites have narrower melting

intervals and lower solidus temperatures than peridotites. Such pyroxenites entrained in an adiabatically upwelling mantle consisting largely of peridotite would contribute a greater fraction of liquid to the aggregated mantle partial melt than would be inferred from their relatively low mass fraction in the region undergoing melting [*Hirschmann and Stolper*, 1996; *Phipps Morgan*, 2001; *Sleep*, 1984; *Stolper and Asimow*, 2007]. For example, *Hirschmann and Stolper* [1996] estimated that a mantle containing 5% pyroxenite and 95% peridotite could generate a magma with ~15% pyroxenite-derived melt, and *Lambart et al.* [2009a] suggested that the proportion of pyroxenite-derived melt in mid-ocean ridge basalts (MORBs) may reach up to 40% along some ridge segments.

4. Numerous observations and models suggest that partial melts from pyroxene-rich lithologies are components in erupted basaltic magmas [e.g., *Day et al.*, 2009; *Hauri*, 1996; *Herzberg*, 2006, 2011; *Hirschmann and Stolper*, 1996; *Hofmann and White*, 1982; *Lassiter et al.*, 2000; *Prinzhofer et al.*, 1989; *Salters and Dick*, 2002; *Sigmarsson et al.*, 1998; *Sobolev et al.*, 2005, 2008]. For example, Hf isotopic compositions, rare earth element distributions, and $(^{230}Th)/(^{238}U)$ disequilibria observed in MORBs have been used to suggest the presence of residual garnet in their mantle sources [e.g., *Beattie*, 1993; *Kay and Gast*, 1973]. Although melting in the garnet stability field of peridotites (at pressures > 2.5 GPa) [*Kinzler*, 1997] is expected to result in amounts of melting [*Iwamori et al.*, 1995; *Robinson and Wood*, 1998; *Shen and Forsyth*, 1995] that would lead to crustal thicknesses substantially greater than that observed for normal oceanic crust (7.1 ± 0.8 km [*White et al.*, 1992]), melt contributions from pyroxenite, where garnet coexisting with liquid extends to lower pressures (down to ~1.7 GPa) [*Kogiso et al.*, 2004a], might explain both the "garnet signature" of MORBs and the observed crustal thicknesses [*Hirschmann and Stolper*, 1996]. Likewise, the HIMU isotopic compositions of oceanic island basalts (OIBs) have been attributed to the presence in their source regions of clinopyroxene-rich metasomatic veins from subducted lithosphere [*Pilet et al.*, 2011] or of carbonated eclogite [*Dasgupta et al.*, 2010]. In another example, *Sobolev et al.* [2007] used olivine phenocryst compositions (e.g., Ni and Mn) to suggest that mantle-derived magmas at mid-ocean ridges, oceans islands, and large igneous provinces are mixtures of melts of peridotite and pyroxenite, where the component derived from pyroxenite melting can vary from 10 to 100% of the mass of the basalt. Finally, silica-poor and iron-rich examples of MORBs [*Lambart et al.*, 2009a, 2013] and the generally high $CaO/Al_2O_3$ and FeO and $TiO_2$ contents of OIBs relative to MORBs [*Hirschmann et al.*, 2003; *Kogiso et al.*, 2003; *Prytulak and Elliott*, 2007] have also been attributed to the melting of a pyroxenite component in their mantle source regions.

Given the potential for pyroxene-rich lithologies to contribute to the observed compositional and isotopic variability of basaltic magmas and the many cases in which partial melts of pyroxenites have been invoked to explain the petrogenesis of specific basalts, it is not surprising that there is a large and growing body of literature that has focused on the melting of pyroxenite-bearing mantle [e.g., *Allègre and Turcotte*, 1986; *Brown and Lesher*, 2014; *Hirschmann and Stolper*, 1996; *Ito and Mahoney*, 2005; *Kimura and Kawabata*, 2015; *Lassiter et al.*, 2000; *Pertermann and Hirschmann*, 2003a; *Phipps Morgan*, 2001; *Prinzhofer et al.*, 1989; *Sleep*, 1984; *Stolper and Asimow*, 2007]. However, because natural pyroxenites span a wide compositional range with a correspondingly wide range of solidus temperatures and phase relations [*Kogiso et al.*, 2004a, and references therein], modeling their contribution to melt production in the mantle requires a robust means for modeling how melt fraction and residual phase proportions vary with temperature, pressure, and bulk chemical composition. While both empirical [e.g., *Grove et al.*, 2013; *Katz et al.*, 2003; *Kinzler and Grove*, 1992a, 1992b; *Longhi*, 2002; *McKenzie and Bickle*, 1988; *Till et al.*, 2012] and thermodynamically based [*Asimow et al.*, 1997, 2001; *Ghiorso et al.*, 2002] parameterizations are available linking these variables for peridotite melting, there has been less work on pyroxenites. In fact, to our knowledge, a functional relationship between melt fraction ($F$) and temperature ($T$) and pressure ($P$) is only available for three different mafic compositions: G2 [*Pertermann and Hirschmann*, 2003a], MIX1G [*Lambart et al.*, 2013], and KG1 [*Shorttle et al.*, 2014]. However, because each of these parameterizations focused on a single composition and is based on experiments that cover a limited range of $P$ and $T$, these empirical models cannot be applied to other compositions or confidently extrapolated in pressure and temperature space.

Although pMELTS [*Ghiorso et al.*, 2002] in principle should provide a means for modeling pyroxenite melting in a precise and internally consistent fashion, in practice, it overestimates for pyroxenites the temperature interval over which melting occurs. For example, the experimentally determined melting interval for the MIX1G
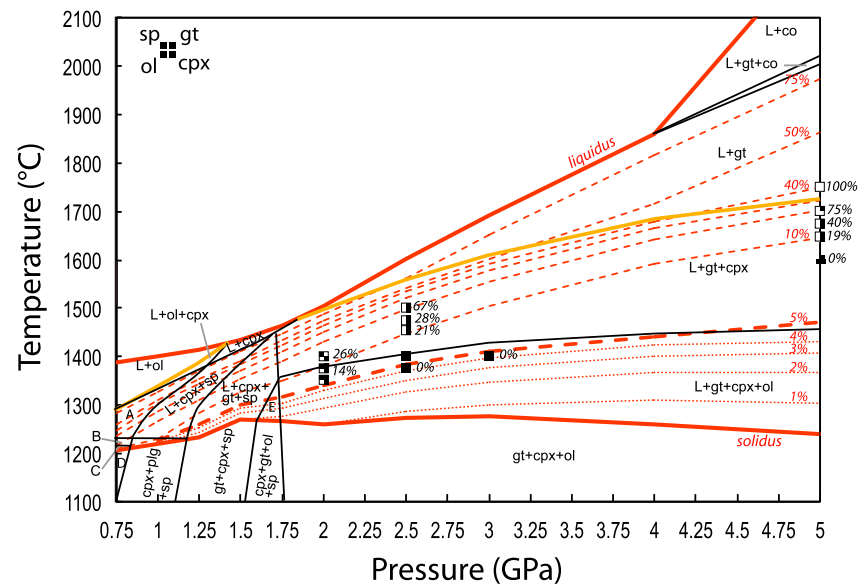
**Figure 1.** Stable phase assemblages calculated with pMELTS [*Ghiorso et al.*, 2002] for the Cr-free pyroxenite composition MIX1G as a function of temperature and pressure. The solidus and liquidus are labeled and shown as heavy red curves. The mass fraction of liquid is contoured in weight percent (dotted or dashed red lines; the 5% melt contour is shown as a heavy dashed red curve); the black lines are contours of stable phase assemblages; the solid orange curve shows the disappearance of cpx. Because $K_2O$ is handled incorrectly in the subsolidus assemblage when feldspar is absent [*Asimow and Ghiorso*, 1998], the location of the solidus in *P-T* space has been calculated for a $K_2O$-free composition; supersolidus calculations included $K_2O$. The negative slope of the calculated solidus is due to the fact that pMELTS does not account for the increasing compatibility of Na in cpx with increasing pressure [e.g., *Jennings and Holland*, 2015]. Abbreviations: L, liquid; ol, olivine; cpx, clinopyroxene; opx, orthopyroxene; sp, spinel; plg, plagioclase; gt, garnet; co, corundum. Capital letters in the phase diagram are for specific assemblages: A = L + ol + cpx + sp, B = L + ol + cpx + plg + sp, C = L + ol + opx + cpx + plg + sp, D = ol + opx + cpx + plg + sp, and E = L + cpx + gt + sp + ol. The split squares at 2, 2.5, 3, and 5 GPa show the experimental phase relations for MIX1G, and the numbers next to the squares are melt percentages [*Hirschmann et al.*, 2003; *Kogiso et al.*, 2003]; the phases present in each experiment are indicated by a black region in the square (key is located in the upper left corner of the figure). Details on the pMELTS calculations can be found in Text S1 in the supporting information.

pyroxenite at 5 GPa is ~150°C [*Kogiso et al.*, 2003]; however, for this composition, pMELTS predicts a melting interval of more than 900°C, and at a given *P* and *T* in the supersolidus region of the phase diagram, pMELTS does not reliably estimate the percentage of melt (Figure 1). These mismatches emphasize the need for a parameterization specific to pyroxenite compositions that is able to accurately predict their *P-T-F* relationships.

In this paper, we present a parameterization for the degree of melting of anhydrous pyroxene-rich rocks as a function of pressure, temperature, and bulk composition (*X*) based on melting experiments on pyroxenites; although our parameterization is empirical, the functional forms of the equations have been guided by pMELTS simulations [*Ghiorso et al.*, 2002]. Although mathematically simple (and therefore incomplete), the parameterization captures important features of the behavior of the melting of pyroxenites—in particular, variations in near-solidus temperature with pressure and bulk composition and, at constant bulk composition, systematic variations in melt fraction with temperature and pressure. Applying the parameterization to melting of a lithologically heterogeneous mantle, we show that contrary to the common assumption that pyroxenite will always start to melt before fertile peridotite in an upwelling mantle, some natural pyroxenite compositions are predicted to have near-solidus temperatures that are greater than that of peridotite at high pressures (i.e., 3–5 GPa). We also discuss how (given certain assumptions about mantle upwelling and melt pooling) this wide range of pyroxenite near-solidus temperatures and variations in melt productivity could influence calculations of crustal thickness for constant mantle potential temperatures.

## 2. Pyroxenite Compositions and Phase Relations

Although a variety of names are used to describe rocks falling under the general heading of "pyroxenite" (e.g., orthopyroxenite, websterite, bronzitite, eclogite), we use the term pyroxenite to refer to mafic and
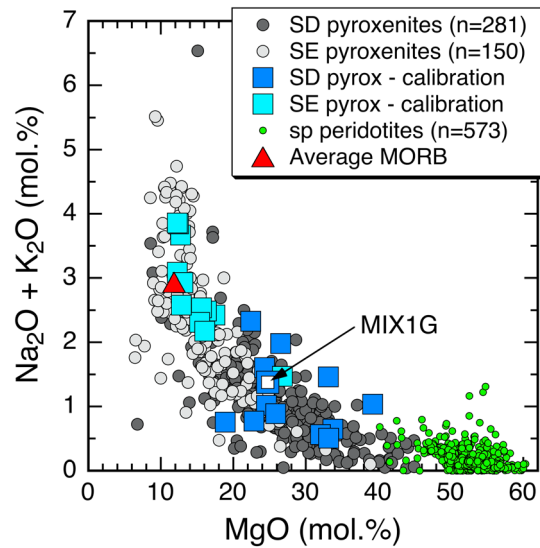
**Figure 2.** $Na_2O + K_2O$ versus MgO (all in oxide mole percent) of natural pyroxenites from ophiolites and alpine-type massifs, gneissic and granulitic massifs, and xenoliths [*Lambart et al.*, 2013, and references therein]; spinel peridotites [*Herzberg et al.*, 1988]; and average MORB [*Gale et al.*, 2013]. See text for the definition of silica-deficient (SD) and silica-excess (SE); pyroxenite compositions (abbreviated pyrox in the legend) whose experimental phase relations were used in the parameterization are shown in two shades of blue (see Table S1 for compositions). The significance of MIX1G [*Hirschmann et al.*, 2003] is discussed in section 3.3.1. Figure S1 in the supporting information shows other oxides (in mole percent) and bulk Mg# [Mg/(Mg + Fe*), molar; Fe* is all Fe as FeO] as a function of MgO (in mole percent).

ultramaficpyroxene-rich plutonic rocks that lack sufficient olivine (40%) to be considered peridotites [*Le Maitre et al.*, 2002]. Depending on composition, garnet often joins pyroxenes as an increasing major constituent of these rocks at pressures of ~1.5 to 2.4 GPa [*Downes*, 2007, and references therein]. Other phases that can be present in pyroxenites include spinel, plagioclase (± alkali feldspar), amphibole, and biotite; less common phases include corundum, sapphirine, apatite, zircon, quartz/coesite, rutile, and/or graphite/diamond [*Irving*, 1980; *Kornprobst et al.*, 1990; *Kuno and Aoki*, 1970; *Pearson et al.*, 1989]. The variations in modal abundances of olivine, pyroxenes, and aluminous phases, and the diverse suite of minor minerals that can constitute pyroxenites, reflect both their compositional range (extending from basalts to peridotites; Figure 2 and Figure S1 in the supporting information) and the range of pressures and temperatures at which they form.

The wide range of major-element compositions exhibited by pyroxenites leads to correspondingly variable phase relations. Experimental phase equilibra of pyroxenites show that at high pressure (> ~1.7 GPa) [*Kogiso et al.*, 2004a; *Lambart et al.*, 2013], there is a thermal divide defined by the Enstatite (En)-Diopside (Di)-Alumina plane which includes garnets and aluminous pyroxene components such as Ca-Tschermak (CaTs) and Mg-Tschermak (MgTs) in the $CaO-MgO-Al_2O_3-SiO_2$ tetrahedron [*O'Hara*, 1972]. This divide separates silica-excess (SE) pyroxenites (i.e., those plotting on the silica-rich side of the En-CaTs join in a projection from Di onto the forsterite (Fo)-CaTs-quartz (Qtz) plane [*Hirschmann et al.*, 2003]) from silica-deficient (SD) pyroxenites (those lying to the silica-poor, i.e., olivine-rich, side of the En-CaTs join). Figure 2 shows that the vast majority of pyroxenites that approach the compositional field of spinel peridotites are silica deficient (see also Figure S1) and that SD pyroxenites are generally enriched in MgO relative to the majority of SE pyroxenites. At the low MgO end of the trend in Figure 2, SE pyroxenites are essentially basaltic in composition. Most rocks referred to as pyroxenites in the literature are in the SD category (Figure 2 and Figures S1 and S2 in the supporting information) [e.g., *Hirschmann et al.*, 2003; *Lambart et al.*, 2013; *Pilet et al.*, 2008]. Silica-deficient pyroxenites usually contain olivine in their subsolidus assemblage, and olivine is often the liquidus phase at low pressure (≤1.5 GPa) [*Lambart et al.*, 2009a]. Low-degree partial melts of SD pyroxenites (and their residual liquids during crystallization) are typically nepheline normative [*Hirschmann et al.*, 2003; *Lambart et al.*, 2013], although the silica content can be highly variable (from 37 to 53 wt %) [*Lambart et al.*, 2013]. Most rocks referred to as eclogites in the literature [e.g., *Hirschmann and Stolper*, 1996; *Schiano et al.*, 2000] are SE pyroxenites as are hybrid orthopyroxene-rich and olivine-free pyroxenites proposed to have been formed by the reaction between a silica-rich melt and peridotite [*Kelemen et al.*, 1998; *Mallik and Dasgupta*, 2013; *Rosenthal et al.*, 2014; *Sobolev et al.*, 2005; *Yaxley and Green*, 1998]. A silica polymorph (quartz or coesite), plagioclase ± alkali feldspar (at P ≤ 3 GPa), and rutile are commonly subsolidus phases in SE pyroxenites, and, depending on bulk alumina content, orthopyroxene or plagioclase is often the liquidus phase at low pressure (≤1.5 GPa) [*Kogiso et al.*, 2004a]. Low-degree partial melts of SE pyroxenites are silica-rich (often with >55 wt % $SiO_2$) and have lower CaO and FeO contents than liquids produced by similar extents of melting of SD pyroxenites [see Figure 8 in *Lambart et al.*, 2013].

To date, there have been few efforts to model systematically pyroxenite solidus temperatures as a function of bulk composition and pressure [*Kogiso and Hirschmann*, 2006; *Kogiso et al.*, 2004a]. *Kogiso et al.* [2004a] showed that at a given pressure, the solidus temperature of a pyroxenite mainly depends on the bulk alkali content and Mg# (the molar Mg/(Mg + Fe*) ratio, where Fe* is all Fe as FeO). As we show below, these two compositional parameters are indeed important in parameterizing pyroxenite solidus temperatures. The link between the liquidus temperature (and thus the width of the melting interval at constant pressure) and pyroxenite bulk composition is, however, less well understood. Based on the results of experimental studies available at the time, *Hirschmann and Stolper* [1996] suggested that eclogites (i.e., SE pyroxenites) might be expected to have smaller melting intervals (and thus higher average melt productivities) than MgO-rich pyroxenites (i.e., SD pyroxenites) (Figure 2). However, subsequent experimental work on a wider range of bulk compositions has blurred this suggested relationship; e.g., the MORB-like SE pyroxenite, G2, has a melting interval of 240°C at 2 GPa [*Pertermann and Hirschmann*, 2003a], while the SD pyroxenite, M7-16, has a melting interval of $< 100$°C at the same pressure [*Lambart et al.*, 2013].

## 3. Constructing an Empirical Model (Melt-PX) to Describe Melt Fractions and Near-Solidus Temperatures for Pyroxenites

Empirical parameterizations of solidus temperatures and melt fractions for peridotites have been used to incorporate melting into geodynamic models [e.g., *Iwamori et al.*, 1995; *Katz et al.*, 2003; *Langmuir et al.*, 1992; *McKenzie and Bickle*, 1988; *Niu and Batiza*, 1991], and, although they may ultimately be replaced by rigorous thermodynamic formulations, they are currently useful in that they can often more accurately reproduce existing experimental data than thermodynamic models [*Katz et al.*, 2003]. This observation largely reflects the fact that thermodynamic models are not actually fit to experimentally determined solidi or melt fractions—such data are outputs or predictions of these models. In contrast, solidus and melt fraction determinations can be explicitly fit using an empirical equation or set of equations [e.g., *Hirschmann*, 2000; *Katz et al.*, 2003]. Nevertheless, although rigorous thermodynamic models such as pMELTS [*Ghiorso et al.*, 2002] cannot currently be used to predict accurately the phase relations of pyroxenites (see Figure 1 and the associated discussion in section 1), they can provide an internally self-consistent set of phase relations that can be used to explore parameters that closely correlate with $F$. Thus, the approach we have taken is to couple the thermodynamic foundations of pMELTS with direct empirical fits to solidi and melt fractions from experiments on a wide range of pyroxenite compositions. Specifically, we used pMELTS to guide our selection of functional forms and significant bulk compositional parameters in each of the equations of our model, and then we used available high-pressure experimental data on pyroxenite melting to regress the coefficients in each of these pMELTS-guided equations. By using pMELTS to guide our understanding of the parameters that influence solidus temperature and melt fraction, we gain confidence that we have not neglected any important compositional parameters or effects. As described below, the model is calibrated on 183 experiments (spanning 25 bulk compositions) in which $F$ was determined up to the exhaustion of clinopyroxene from the residue (cpx-out) for pyroxenites over a pressure and temperature range of 0.9–5 GPa and 1150–1675°C.

### 3.1. Modeling Strategy

At each pressure, we are interested in the temperature at which melt first appears on heating the pyroxenite (i.e., the solidus, where $F = 0$%), the temperature and melt fraction at which each crystalline phase appears or disappears, and the temperature at which the pyroxenite is totally molten (i.e., the liquidus, where $F = 100$%). Given the current experimental data set, such a complete characterization of melting is not possible—instead, we have parameterized two important points at each pressure: the temperature at which a pyroxenite bulk composition is 5% molten ($T_{5\%}$) and the temperature at which high-Ca clinopyroxene is exhausted from the residue ($T_{\text{cpx-out}}$).

We have focused on the $F = 5$% isopleth rather than the solidus for three reasons:

1. Precise experimental determination of the solidus of a naturally occurring rock composition (i.e., $T$ at the first appearance of melt in a system with high variance) can be challenging due to the difficulty in visually identifying liquid at low melt fractions (i.e., $F < 1$%). Melt extraction techniques (e.g., the diamond aggregate and the microdyke techniques) [*Baker and Stolper*, 1994; *Baker et al.*, 1995; *Hirose and Kushiro*, 1993; *Johnson and Kushiro*, 1992; *Lambart et al.*, 2012; *Laporte et al.*, 2004] can aid in detecting near-solidus

partial melts in high-pressure experimental charges, but these techniques have not been widely used in the study of pyroxenite melting (exceptions are the studies of *Hirschmann et al.* [2003], *Kogiso et al.* [1998], *Lambart et al.* [2009a, 2012, 2013], *Pertermann and Hirschmann* [2003a, 2003b], and *Spandler et al.* [2008]). Given the considerable uncertainty in detecting the solidus, there is potentially a lack of consistency among the results of different investigators. For example, as noted by *Hirschmann* [2000], experimentally determined solidus temperatures at 1.5 GPa for the peridotite KLB-1 differ by 60°C between the studies of *Hirose and Kushiro* [1993] and *Takahashi et al.* [1993]. In contrast, at 5% melting, quenched melt is relatively easy to identify and quantify [*Laporte et al.*, 2004].

2. Second, minor subsolidus phases (e.g., phosphates, silica, and kyanite) can result in a significant depression of the solidus to something close to eutectic- or peritectic-like melting involving these minor phases—such melting reactions are largely disconnected from significant variations in the major-element composition of the rock [e.g., *Pertermann and Hirschmann*, 2003a; *Spandler et al.*, 2008]. For example, the addition of 2000 ppm $P_2O_5$ to the MM3 peridotite composition [*Baker and Stolper*, 1994] stabilizes whitlockite and causes a ~30°C drop in the pMELTS-predicted solidus at 2 GPa compared to that for the phosphorus-free composition; at $F = 5\%$, whitlockite is not stable and the temperature difference between the P-bearing and P-free compositions is only 12°C.

3. Finally, volatiles such as $H_2O$ and $CO_2$ are often not well characterized for a given experiment and can reach sufficiently high concentrations in low melt fraction liquids so as to substantially lower the solidus relative to the volatile-free case [*Falloon and Danyushevsky*, 2000; *Gaetani and Grove*, 1998; *Hirschmann et al.*, 1999; *Médard and Grove*, 2008]. This depression of the solidus is uncorrelated with the major-element composition of the rock and can be very large. For example, at 2 GPa and bulk water contents of 0 to 700 ppm, pMELTS predicts a solidus temperature variation of almost 400°C for MM3. This range of water contents easily spans nominally anhydrous mantle melting experiments, including those where an effort was made to minimize the amount of adsorbed water on the starting materials [*Falloon et al.*, 2001; *Hirschmann et al.*, 1998a; *Lambart et al.*, 2009b; *Laporte et al.*, 2004, 2014; *Wasylenki et al.*, 2003]. In contrast, the calculated spread in temperatures required to generate 5% melting of MM3 at 2 GPa with the same range of water contents is only 56°C. Thus, by only considering melt fractions ≥5%, we minimize the potentially confounding effects of water and other minor incompatible elements on the estimations of melt fractions near the solidus. There are petrological problems for which these variations in solidus temperature and melt fractions of <1% are important (e.g., mantle rheology, the mobility of low-degree melts, and resulting metasomatism), so our results will be of more value for problems in which larger amounts of melting are involved.

In addition to parameterizing $T_{5\%}$ for pyroxenite compositions, we also parameterized $T_{cpx-out}$, the temperature at which high-Ca clinopyroxene is exhausted from the residue. Clinopyroxene is a major modal phase (typically dominant) in nearly all pyroxenites, and for the range of pressures considered here, clinopyroxene is either the liquidus phase or one that disappears at high degrees of melting (see Figure 1 and Figures S3 and S4 in the supporting information). Thus, clinopyroxene exhaustion at high melt fractions is also a petrologically significant marker in the melting of pyroxene-rich mantle lithologies. Additionally, because this phase boundary occurs for most experimentally studied pyroxenites and is relatively easy to detect experimentally, it can be parameterized over most of the wide range of compositions represented in our experimental database (Figures S3 and S4 in the supporting information).

Note that both the cpx-out boundary (the orange curve in Figure 1) and the 5% melt isopleth (the thick dashed red curve in Figure 1) are associated with varying phase assemblages as pressure increases and that discontinuities along these paths in *P-T* space accompany these changes in phase assemblage. Nevertheless, Figure 1 also shows that even considering these discontinuities, these boundaries can be well approximated as continuous curves; consequently, we neglect this complexity as it would require significantly more parameters to fit these discontinuities without much improvement in the quality of the overall fits. In section 3.5, we will evaluate the applicability of the assumption that we can use smoothly varying, continuous functions of *T*, *P*, and *X* to describe $T_{5\%}$ and $T_{cpx-out}$ by examining the degree to which such functions fit the available phase equilibria data.

We have not attempted to fit the liquidus as a function of *T*, *P*, and *X*. Our principal reasons are as follows: (1) as shown in Figure 1, the discontinuities with phase changes along the liquidus are greater than those for the solidus and cpx-out curves making it more difficult to fit the liquidus without large numbers of additional

parameters and (2) the liquidus is of less importance for petrological questions involving the role of pyroxenite melting during petrogenesis, most of which involve less than complete melting. However, we will address how well our parameterization does when extrapolated to temperatures above cpx-out.

### 3.2. Structure of the Parameterization

For any given pyroxenite, we assume that for isobaric melting between $F = 5\%$ and $F$ at cpx-out, melt fraction is a concave upward, quadratic function of temperature. This assumption is consistent with the parameterization developed for the pyroxenite G2 [see Figure 5 in *Pertermann and Hirschmann*, 2003a] and with the results of pMELTS calculations on various pyroxenite bulk compositions (Figure S5). A concave upward quadratic form is also consistent with the experimentally observed increase in isobaric melt productivity with increasing $F$ during pyroxenite melting (at least until the exhaustion of clinopyroxene) [*Lambart et al.*, 2009a; *Sobolev et al.*, 2007; *Spandler et al.*, 2008]. Finally, MELTS calculations using peridotite compositions also show a concave upward quadratic trend for $F$ versus $T$ between $F = 5\%$ and $F$ at cpx-out [*Hirschmann et al.*, 1998b].

In terms of dimensionless temperature ($T'$), our quadratic parameterization of melting is written as follows:

$$F = A \cdot T'^2 + B \cdot T' + 5 \quad \text{with} \quad T' = (T - T_{5\%})/(T_{cpx-out} - T_{5\%}), \tag{1}$$

where $F$ is the weight fraction of melt, $T_{5\%}$ is the temperature at $F = 5\%$, $T_{cpx-out}$ is the temperature of clinopyroxene exhaustion in the pyroxenite assemblage, and A and B are functions of the pressure ($P$, in GPa) and the bulk composition of the pyroxenite. As discussed above and further elaborated below, the model is constructed in three steps by determining four functional relationships: (1) $T_{5\%} = f(P, X)$, (2) $T_{cpx-out} = f(P, X)$, and (3) the functional forms of A and B in equation (1).

In the following sections, we describe the specifics of the pMELTS simulations and how we used them to constrain the functional forms of $T_{5\%}$, $T_{cpx-out}$, A, and B; the experimental data we used to constrain the coefficients in each equation; the results of our least squares fits to these experimental data; and an evaluation of the model and its limitations.

### 3.3. Mathematical Formulation

Here we discuss the first of the tasks mentioned above—using pMELTS [*Ghiorso et al.*, 2002]—to determine which compositional components most strongly correlate with $T_{5\%}$, $T_{cpx-out}$, and A and B and to guide our choice of functional forms for their variations. Details of the pMELTS calculations are presented in Text S1 in the supporting information.

#### 3.3.1. Temperatures at $F = 5\%$

Starting with MIX1G [*Hirschmann et al.*, 2003], which is close to the average of the pyroxenite compositions plotted in Figure 2, we generated 36 modified compositions by independently varying the molar contents of $Na_2O$ and $SiO_2$, the Mg#, the molar $CaO/Al_2O_3$ ratio, and the distance to the garnet-pyroxene plane (by varying the forsterite (Fo) and the quartz (Qz) components using expressions in *O'Hara* [1972]) so as to cover the range of experimental compositions in our database. We then used pMELTS to calculate $T_{5\%}$ for each of these compositions at 1–5 GPa so as to identify the most significant variables that correlate with $T_{5\%}$. This exercise yielded 143 synthetic $T_{5\%}$ values—for some compositions, pMELTS "crashed" before reaching 5% melt or yielded a negative $dT_{5\%}/dP$ slope at high pressures (e.g., MIX1G in Figure 1; an artifact of pMELTS as noted above).

Figure 3 shows the results of a subset of these calculations. Consistent with experimental observations on pyroxenites [*Kogiso and Hirschmann*, 2006] and previous studies on peridotites (see references in *Hirschmann* [2000]), bulk $Na_2O + K_2O$ content (in mole percent, referred to as "alk"), bulk Mg#, and $P$ are the three parameters that most strongly correlate with $T_{5\%}$ (because $K_2O$ is handled incorrectly in the subsolidus assemblage when feldspar is absent [*Asimow and Ghiorso*, 1998], $K_2O$ content was held constant in our simulations; see Text S1 in the supporting information). A detailed discussion of the effect of each tested parameter on $T_{5\%}$ is presented in Text S3 in the supporting information. Combining the linear dependence of $T_{5\%}$ on Mg# and molar $Na_2O + K_2O$ (Figures 3a and 3b), with the observation that $T_{5\%}$ is best represented by a quadratic function in pressure (Figure 3c), suggests the following expression:

$$T_{5\%} = P^2 \cdot (a \cdot (Na_2O + K_2O) + b) + P \cdot (c \cdot (Na_2O + K_2O) + d \cdot Mg\# + e) + f, \tag{2}$$
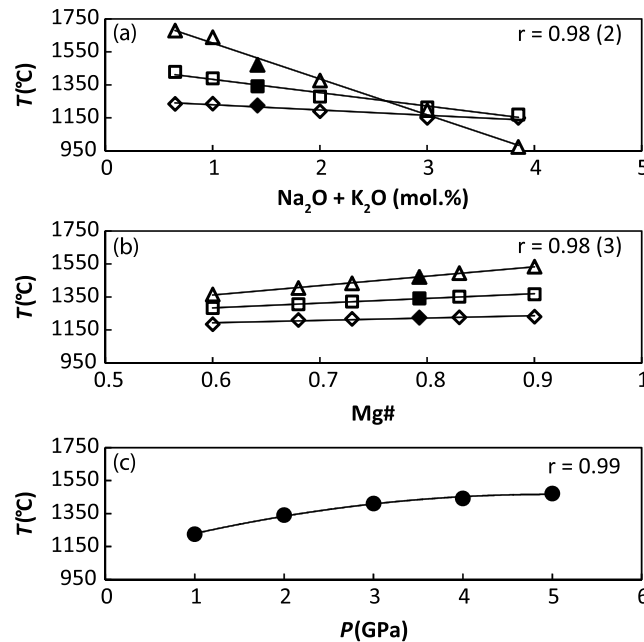
**Figure 3.** Calculated $T_{5\%}$ for MIX1G and derivative compositions at 1 GPa (diamonds), 2 GPa (squares), and 5 GPa (triangles) versus (a) the bulk $Na_2O + K_2O$ content (molar) and (b) the Mg#. The composition MIX1G is shown by the filled symbols in each panel. (c) Calculated $T_{5\%}$ for MIX1G as a function of pressure. In Figures 3a and 3b, straight lines are the best linear fits, and $r$ is the average of the correlation coefficients calculated at each pressure; the $1\sigma$ deviation (in parentheses) is given in terms of the least unit cited. In Figure 3c, the curve is the best quadratic fit and $r$ is the corresponding correlation coefficient. All calculations were done using pMELTS.

where a, b, …, f are constants, $P$ is in GPa, and $Na_2O$ and $K_2O$ are in mole percent. We fit the 143 synthetic $T_{5\%}$ values calculated using pMELTS to equation (2); the resulting best fit accounts for 98% of the variance in the synthetic $T_{5\%}$ values.

### 3.3.2. Temperature at cpx Disappearance

We followed a similar procedure to that for $T_{5\%}$ to find an acceptable functional form for $T_{cpx-out}$. The 143 pMELTS calculations show that $T_{cpx-out}$ is a strong function of pressure—in fact, a quadratic function in $P$ accounts for 91% of the variance in $T_{cpx-out}$ independent of any compositional terms. The same quadratic expression when used to fit the experimental data set (discussed in detail in section 3.4) accounts for ~75% of the observed variance in $T_{cpx-out}$. For the synthetic pMELTS data set, no compositional parameters substantially improved the fit to $T_{cpx-out}$, but including Mg# and bulk $Al_2O_3$ and CaO molar contents significantly improved the fit to $T_{cpx-out}$ for the experimental data set. The resulting expression is as follows:

$$T_{cpx-out} = a' \cdot P^2 + b' \cdot P + c' \cdot Mg\# + d' \cdot Al_2O_3 + e' \cdot CaO + f', \tag{3}$$

where a', b', … f ' are constants and $Al_2O_3$ and CaO are in mole percent. Equation (3) accounts for 90% of the variance in $T_{cpx-out}$ in the experimental data set. Refitting the synthetic pMELTS data using this expression accounts for 92% of the variance and produces a small drop in the standard error of estimate (SEE) for the fit, from 17°C (using just pressure) to 14°C.

### 3.3.3. The Relationship Between *F-P-T* for Mantle Pyroxenites

The previous two sections described our parameterizations of $T_{5\%}$ and $T_{cpx-out}$, both of which are necessary to compute $F$ versus $T$ and $P$ using equation (1). The next step is to determine which parameters most strongly control the functions A and B in equation (1). Combined with the parameterizations of $T_{5\%}$ and $T_{cpx-out}$, this will allow the calculation of $F$ (up to cpx-out) as a function of $T$, $P$, and $X$ over the range of conditions and compositions covered by the available experiments.

Functions A and B are simply related to the melt fraction at cpx-out, i.e., substituting $T_{cpx-out}$ for $T$ in equation (1) yields

$$F(T_{cpx-out}) = A + B + 5. \tag{4}$$

Consequently, equations for A and B can be constrained by examining how $F(T_{cpx-out})$ varies with $P$ and $X$.

While pMELTS substantially overestimates the effect of pressure on $F(T_{cpx-out})$ relative to what is observed in experimental results (e.g., between 2 and 5 GPa, $F(T_{cpx-out})$ decreases from 100 to 39.5 wt % in the pMELTS calculations on MIX1G versus from 100 to 76 wt % in the actual MIX1G experiments), calculated and experimental data on composition MIX1G are qualitatively consistent in that both show clinopyroxene on the liquidus at ~2 GPa (i.e., $F(T_{cpx-out}) = 100$) and both show that garnet replaces clinopyroxene as the liquidus phase with increasing pressure (Figure 1). At a given pressure, $F(T_{cpx-out})$ will be controlled by the modal abundance
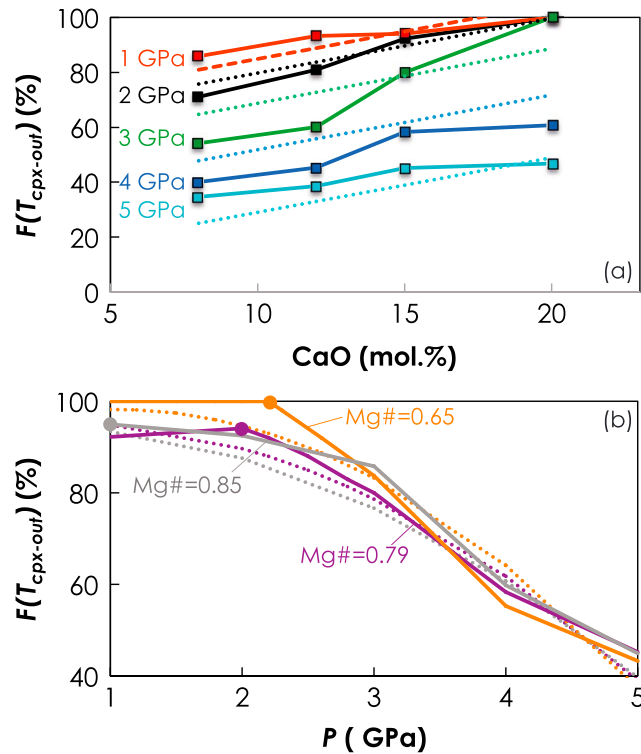
**Figure 4.** Relationship between $F(T_{cpx-out})$ and (a) bulk molar CaO contents and pressure, and (b) pressure and bulk Mg# based on pMELTS calculations on pyroxenite compositions derived from MIX1G as described in the text. In both panels, solid lines connect $F(T_{cpx-out})$ values calculated using pMELTS and dashed lines show $F(T_{cpx-out})$ values calculated using the best fits of the pMELTS-calculated values of $F(T_{cpx-out})$ to equations 4–6. In Figure 4a, all four compositions have Mg# = 0.79; in Figure 4b all three bulk compositions contained 15 mol % CaO. Circles associated with the solid lines indicate the maximum value for $F(T_{cpx-out})$.

of clinopyroxene and the isobaric rate at which clinopyroxene melts. Note that modal abundances are strongly correlated with normative clinopyroxene abundances and bulk CaO contents. Figure 4a shows this relationship for a subset of the synthetic data from the pMELTS simulations. At a given pressure, $F(T_{cpx-out})$ is highly correlated with the CaO content, in mole percent, in the synthetic pyroxenite compositions. The pMELTS simulations also show that $F(T_{cpx-out})$ for a wide range of pyroxenite compositions reaches a maximum at pressures between 1 and 2.5 GPa and then decreases with further increases in pressure in response to the expansion of the garnet phase volume (Figure 4b). This concave down shape of $F(T_{cpx-out})$ as a function of pressure suggests as a first approximation a quadratic pressure dependence for $F(T_{cpx-out})$. Finally, although Mg# does not have a significant effect on the curvature of $F(T_{cpx-out})$ as a function of $P$, the pressure at which $F(T_{cpx-out})$ reaches a maximum decreases with increasing Mg# (Figure 4b).

In summary, the three parameters that influence $F(T_{cpx-out})$ most strongly and, consequently, the parameters in equation (4) are as follows: $P$, the bulk CaO content, and the Mg#. Based on these insights, we explored several different functional forms for A and B using these parameters and a trial and error approach in order to find expressions for A and B that allow equation (4) to satisfy the constraints provided by both calculated (pMELTS) and experimental $F(T_{cpx-out})$ values and the requirement that $F$ between 5% and $T_{cpx-out}$ be a concave up, quadratic function of temperature over the pressure range of 0.9 to 5 GPa for all compositions in the experimental data set. The following expressions for A and B satisfy all these constraints, account for 91% of the variance in the synthetic $F(T_{cpx-out})$ values, and reproduced the experimental $F(T_{cpx-out})$ with a SEE of 8% absolute (see section 3.5):

$$A = (A' + B' \cdot Mg\#) \cdot P^2 + (C' + D' \cdot Mg\#) \cdot P + E', \quad (5)$$

$$B = A'' \cdot CaO + B'', \quad (6)$$

where the coefficients A' through E' and A'' and B'' are constants and CaO is in mole percent.

### 3.4. Experimental Database

We have calibrated our model using nominally anhydrous high-pressure experiments on 25 pyroxenite compositions (14 SD pyroxenites, 10 SE pyroxenites, and 1 bimineralic pyroxenite) from 11 different laboratories. In order to maximize the likelihood that all of the experiments included in our data set maintained constant bulk composition (volatiles excluded), we only selected experiments performed in double graphite-platinum capsules. The inner graphite capsule prevents Fe loss to the outer Pt capsule and limits oxygen fugacity to a relatively narrow band in $T$-$fO_2$ space (QFM−2.3 ± 0.3) [*Médard et al.*, 2008].

**Table 1.** Summary of Functional Forms, Parameters, and Values[a]

| Functional Forms | | | Equation |
|---|---|---|---|
| $F = A \cdot T'^2 + B \cdot T' + 5$ | | | (1) |
| $T' = (T - T_{5\%})/(T_{\text{cpx-out}} - T_{5\%})$ | | | |
| $T_{5\%} = (a \cdot [\text{alk}] + b) \cdot P^2 + (c \cdot [\text{alk}] + d \cdot \text{Mg\#} + e) \cdot P + f$ | | | (2) |
| $T_{\text{cpx-out}} = a' \cdot P^2 + b' \cdot P + c' \cdot \text{Mg\#} + d' \cdot Al_2O_3 + e' \cdot CaO + f'$ | | | (3) |
| $A = (A' + B' \cdot \text{Mg\#}) \cdot P^2 + (C' + D' \cdot \text{Mg\#}) \cdot P + E'$ | | | (5) |
| $B = A'' \cdot CaO + B''$ | | | (6) |

| Parameters | For Calculating | Value | Unit |
|---|---|---|---|
| a | $T_{5\%}$ | 1.40 | °C mol$^{-1}$ GPa$^{-2}$ |
| b | | −7.08 | °C GPa$^{-2}$ |
| c | | −12.5 | °C mol$^{-1}$ GPa$^{-1}$ |
| d | | 150 | °C GPa$^{-1}$ |
| e | | 25.5 | °C GPa$^{-1}$ |
| f | | 1105 | °C |
| a′ | $T_{\text{cpx-out}}$ | −14 | °C GPa$^{-2}$ |
| b′ | | 177 | °C GPa$^{-1}$ |
| c′ | | 219 | °C |
| d′ | | −17.2 | °C mol$^{-1}$ |
| e′ | | 10.4 | °C mol$^{-1}$ |
| f′ | | 1000 | °C |
| A′ | A | −2.63 | GPa$^{-2}$ |
| B′ | | −1.58 | GPa$^{-2}$ |
| C′ | | 26.9 | GPa$^{-1}$ |
| D′ | | −7.5 | GPa$^{-1}$ |
| E′ | | 4.23 | - |
| A″ | B | 2.86 | mol$^{-1}$ |
| B″ | | 18 | - |

[a]Abbreviations: $F$ is the melt fraction (in weight percent), $T_{5\%}$ is the temperature at $F = 5$ wt % (in °C), $T_{\text{cpx-out}}$ is the temperature at which clinopyroxene disappears in the assemblage, $P$ is the pressure in GPa, Mg# is the molar ratio Mg/(Mg + Fe*) where Fe* is all Fe as Fe$^{2+}$, [alk] is the sum of Na$_2$O and K$_2$O in mole percent, and CaO, Na$_2$O, K$_2$O, and Al$_2$O$_3$ are the contents (in mole percent) of these oxides in the bulk-rock composition.

In order to generate a consistent set of melt fractions for all of the experiments in our data set, we recalculated $F$ and its uncertainty ($2\sigma$) for each experiment using the nonlinear approach to mass balance of *Albarède and Provost* [1977]; the mass balance calculations for each experiment were based on the concentrations of seven oxides (SiO$_2$-TiO$_2$-Al$_2$O$_3$-FeO*-MgO-CaO-Na$_2$O) in coexisting melt and solid phases in each experiment for which such data were available. Overall, the recalculated $F$ values are close to those reported in each of the studies included in our database (the average deviation is ~3% relative). For the seven experiments performed on the composition Px-1 [*Sobolev et al.*, 2007], we did not have access to the solid phase compositions, so we used the melt fractions and the $T_{\text{cpx-out}}$ values reported by the authors (calculated with an unspecified least squares method); these data showed no systematic offset relative to other experiments used in the final fit. For each set of experiments (where a "set" refers to all experiments performed on a given composition at a given pressure), we plotted the experimental temperatures as a function of the recalculated melt percentages and used a quadratic regression to estimate $T$ (and its uncertainty) at $F = 5$% and at cpx-out. Linear fits to the calculated proportions of clinopyroxene as a function of $F$ allowed us to estimate $F(T_{\text{cpx-out}})$ (see Text S2 in the supporting information for more details). Experiments on 18 pyroxenites (each with a different bulk composition) were used to calibrate $T_{5\%}$ and $F(T_{\text{cpx-out}})$ (Table S1). Seven studies on pyroxenites where $T_{\text{cpx-out}}$ was closely bracketed but $F$ not determined (Table S1) were also included in the database, yielding a total of 41 $T_{5\%}$ values, 55 $T_{\text{cpx-out}}$ values, and 35 $F(T_{\text{cpx-out}})$ values (all compositions used in the calibration are shown as dark and light blue squares in Figure 2).

### 3.5. Model Calibration

Best fit values for the 19 coefficients in equations (1), (2), (3), (5), and (6) were calculated by minimizing the sum of the squares between the experimental and model values ($T_{5\%}$, $T_{\text{cpx-out}}$, $F(T_{\text{cpx-out}})$, or $F$) using weighted fits. We first determined initial best fit values for the coefficients in equation (2) (i.e., $T_{5\%}$) and equation (3) (i.e., $T_{\text{cpx-out}}$). We then inserted equations (5) and (6) into equation (1) and solved for the coefficients that define A and B (coefficients for equations (2) and (3) were held constant). Equation (4) and values for $F(T_{\text{cpx-out}})$ allowed us to check and further refine the coefficients in equations (5) and (6). This was followed by repeated minimizations of equation (1) holding subsets of the coefficients constant (for equations (2), (3), (5), and (6)) allowing us to optimize the coefficients for all sets of equations (solving simultaneously for all the coefficients in equation (1) yielded coefficients that produced a good fit to the global set of $F$ values but relatively poor fits to $T_{5\%}$, $T_{\text{cpx-out}}$, and $F(T_{\text{cpx-out}})$, i.e., equations 2–4). The optimized coefficients are reported in Table 1.
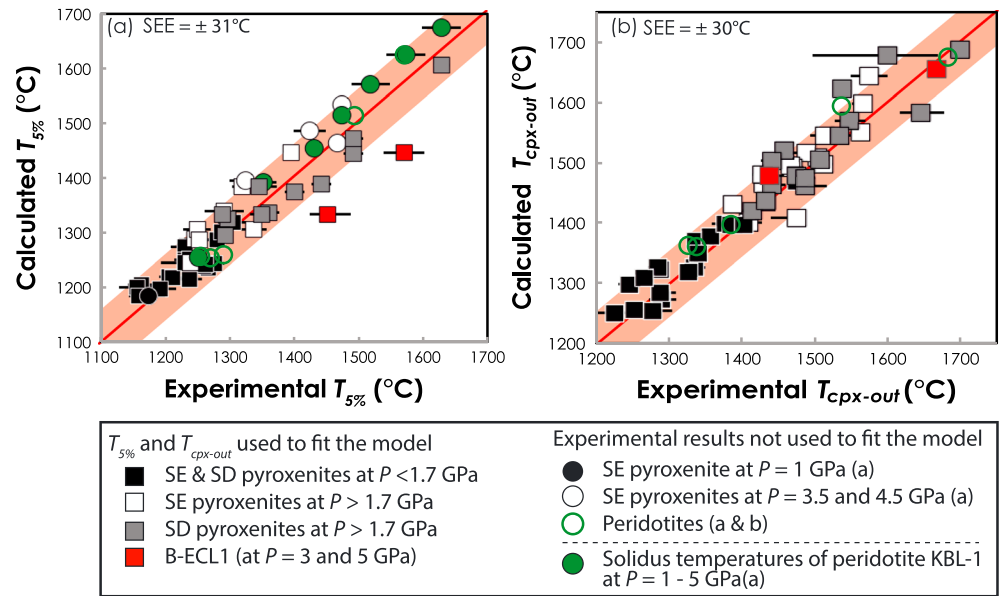
**Figure 5.** Comparison of (a) $T_{5\%}$ and (b) $T_{cpx-out}$ calculated with equations (2) and (3), respectively, with $T_{5\%}$ and $T_{cpx-out}$ based on experimental results. The red line is the 1:1 line, and the orange band indicates the two SEE uncertainties. When not visible, the error bars ($2\sigma$) on the experimental values are smaller than the symbols. Black squares are <1.7 GPa experiments (both SE and SD pyroxenites); white squares are experiments performed above 1.7 GPa on SE pyroxenites; gray squares are experiments performed above 1.7 GPa on SD pyroxenites (1.7 GPa represents a convenient pressure demarcation—the thermal divide appears at ~1.7 GPa); red squares are experiments performed at 3 and 5 GPa on the bimineralogic eclogite B-ECL1. In Figure 5a, black and white circles are experimental results not included in the model (the solidus was only closely bracketed—we assume that the temperature brackets either encompass or are close to $T_{5\%}$; see text for more details): black circle is CRB72-31 at 1 GPa [*Takahashi et al.*, 1998]; white circles are Gb108 at 3.5 and 4.5 GPa [*Yaxley and Sobolev*, 2007] and GA1$_{50}$MPY90$_{50}$ and GA1$_{25}$MPY90$_{75}$ at 3.5 GPa [*Yaxley*, 2000]; filled green circles are bracketed solidus temperatures (not included in the fit) for peridotite KBL-1 [*Herzberg et al.*, 2000, and references therein] from 1 to 5 GPa (see section 4.3). In Figures 5a and 5b, open green circles are $T_{5\%}$ and $T_{cpx-out}$ for DMM1 [*Wasylenki et al.*, 2003], MM3 [*Baker and Stolper*, 1994], and FERB [*Pickering-Witter and Johnston*, 2000] at 1 GPa, and KR4003 [*Walter*, 1998] at 3 and 4 GPa (see section 4.3).

Equation (2) explains 85% of the experimental variance and reproduces the input $T_{5\%}$ values with a mean absolute error of ~31°C over a total temperature range of ~500°C (Figure 5a). The two experimental values that do not fall within the two SEE bounds of the model are for the composition B-ECL1 (see below). Equation (3) explains 90% of the experimental variance and reproduces the input $T_{cpx-out}$ with a mean absolute error of ~30°C; the maximum misfit is 72°C (Figure 5b). Given the uncertainties on $T_{cpx-out}$, all of the experimental values fall within the two SEE bounds. Equation (4) combined with equations (5) and (6) reproduces $F(T_{cpx-out})$ with a SEE of 8% absolute (Figure 6a), while equation (1) reproduces the input $F$ values with a SEE of 13% absolute and explains 80% of the experimental variance (Figure 6b). This percentage of the explained variance in $F$ is similar to those obtained with parameterizations of peridotite melting (72–85%) [see Table 3 on *Katz et al.*, 2003] and is much higher than the value obtained (55%) when pMELTS is used to calculate melt fractions at the $P$ and $T$ of each experiment. Finally, values of SEE on the fits to $T_{5\%}$, $T_{cpx-out}$, and $F$ need to be considered in light of the temperature and pressure uncertainties associated with the piston-cylinder and multianvil apparatuses. Although pressure and temperature uncertainties associated with the piston-cylinder are typically reported as approximately 0.1 GPa and 10–15°C, interlaboratory variability is likely to be much larger [e.g., *Longhi*, 2005], and pressure and temperature uncertainties for multianvil experiments (comprising ~5% of our database, all at $P \geq 3$ GPa) are certainly much larger (routine estimates are 0.2–0.3 GPa and 40–50°C) [e.g., *Kogiso et al.*, 2003; *Takahashi et al.*, 1993; *Walter*, 1998]. These experimental uncertainties place ultimate limits on the goodness of fit of any model that uses a global data set that includes experiments from multiple laboratories.

As a test of our model, we used equation (2) to calculate $T_{5\%}$ values for five experiments on three pyroxenite compositions (1 to 4.5 GPa; black and white filled circles in Figure 5a) that had not been used in fitting the
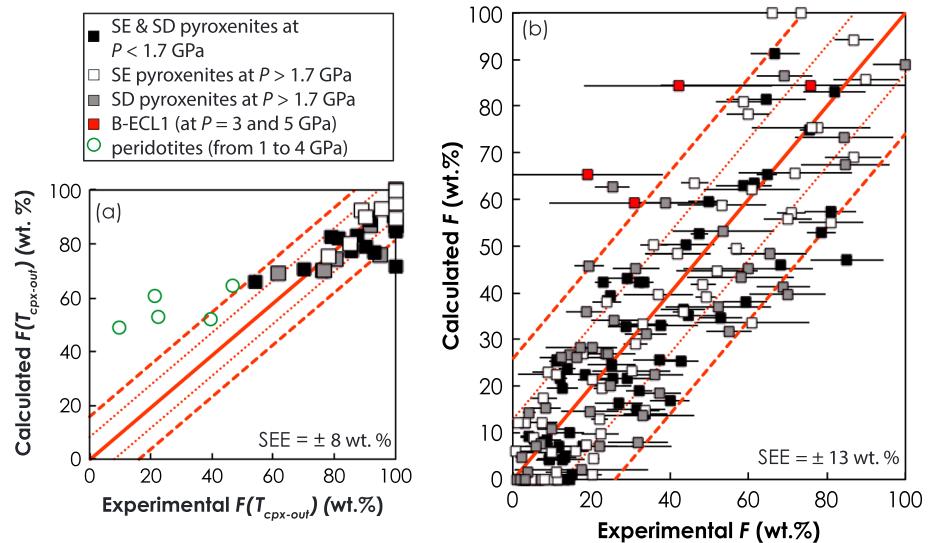
**Figure 6.** (a) Comparison between $F(T_{cpx-out})$ calculated using equation (4) combined with equations (5) and (6) and $F(T_{cpx-out})$ based on experimental results (Table S1). (b) Comparison between $F$ calculated using our parameterization (equation (1)) and melt percentages from the experiments used to calibrate the model. When not visible, the error bars ($2\sigma$) on the experimental $F$ values are smaller than the symbols. The solid red line is the 1:1 line; the dotted and dashed red lines are model uncertainties at ±1 SEE and ±2 SEE, respectively. In Figure 6a, open green circles are $F(T_{cpx-out})$ for the peridotites DMM1 [*Wasylenki et al.*, 2003], MM3 [*Baker and Stolper*, 1994], and FERB [*Pickering-Witter and Johnston*, 2000] at 1 GPa and KR4003 [*Walter*, 1998] at 3 and 4 GPa (see section 4.3). Same symbol color scheme as in Figure 5.

coefficients. For these nominally anhydrous, double-capsule experiments, the solidus was only visually bracketed and we assumed that $T_{5\%}$ lays midway between the highest temperature subsolidus run and the lowest temperature supersolidus run. In all cases, the experimentally estimated value for $T_{5\%}$ lies within the two SEE bounds of our model (Figure 5a). Additional tests indicating that our equations include the significant variables that influence $T_{5\%}$, $T_{cpx-out}$, and $F$ for all the pyroxenite compositions in the experimental data set (with the possible exception of those lying right on the thermal divide; see next paragraph) can be found in Text S4 in the supporting information.

The largest discrepancies in calculated $T_{5\%}$ and $F$ values are for the composition B-ECL1 at 3 GPa for which $T_{5\%}$ is underestimated by 113°C (Figure 5a) and $F$ overestimated by 42–46% absolute (Figure 6b). B-ECL1 is a bimineralogic eclogite positioned on the Enstatite-Diopside-Alumina plane (i.e., the thermal divide). Because the solidus temperature of a composition on a thermal divide must be higher than those of compositions on either side of the divide, it is possible that the underestimated $T_{5\%}$ values for B-ECL1 reflect the fact that our model does not properly account for this increase in solidus temperature for compositions very near the thermal divide (see Text S3 in the supporting information). Nevertheless, such compositions are rare in our pyroxenite compilation (only 34 of the 431 compositions plotted in Figure 2 lie on or close to the thermal divide, i.e., within ±1% Qz; Qz = 0 along the divide in the tetrahedron Qz-Wollastonite-$Al_2O_3$-Enstatite). Although our model systematically overestimates $F$ for composition B-ECL1 at 3 and 5 GPa (Figure 6b) (because $T_{5\%}$ is systematically underestimated), we note that the $2\sigma$ errors on the percentage of melt in all four of the experiments are large (from 20% to 38% absolute, respectively), and when these errors are considered, three of the four points (the red squares in Figure 6b) overlap with the two SEE bounds of the model and the fourth point nearly does so.

As shown in Figures 5 and 6, equations (1) through (6) capture many of the fundamental characteristics of pyroxenite melting—these equations are incorporated into an Excel spreadsheet, Melt-PX, which is available in the supporting information; a detailed explanation of its use is given in Appendix A.

## 4. Extrapolation and Limitations of the Parameterization

As discussed above, Melt-PX is calibrated for pyroxenites (Figures 2 and S1) at pressures between 0.9 and 5 GPa and for degrees of melting between 5% and that defined by the disappearance of clinopyroxene.

Here we discuss, in general terms, the extent to which the model can be extrapolated to compositions outside the range of those used in the calibration and to calculated temperatures outside the range $T_{5\%}$ to $T_{\text{cpx-out}}$.

### 4.1. Extrapolating Beyond the Interval Between $T_{5\%}$ and $T_{\text{cpx-out}}$

As we discussed above, the relationship between melt fraction and temperature just above the solidus is likely to be strongly influenced by minor crystalline phases (e.g., phosphates, quartz, or coesite) and/or components in the bulk composition such as $H_2O$ and $CO_2$ that are highly compatible in a partial melt. For this reason, the model will generally become increasingly inaccurate as $F$ approaches zero and should be used cautiously under $P$-$T$ conditions that generate $<5\%$ melt.

For $F > F(T_{\text{cpx-out}})$, the drop in melt productivity that occurs with the disappearance of a phase [*Asimow et al.*, 1997] must introduce a systematic error when we extrapolate the model beyond cpx-out since our $F$ versus $T$ functions do not have discontinuities in isobaric melt productivity, $(\partial F/\partial T)_P$. Nevertheless, for pyroxenites, this effect seems to be most dramatic at low pressures. For example, in the 1 GPa experiments of *Lambart et al.* [2009a] on M5-40 and M7-16, pyroxenites with between 19 and 24 mol % MgO (Table S1), $(\partial F/\partial T)_P$ decreases by over a factor of 2 with the disappearance of clinopyroxene: 1 to 0.4 and 0.9 to 0.2%/°C, respectively. As discussed above, at intermediate pressures (2–3 GPa) clinopyroxene is the liquidus phase for most pyroxenites and, in such cases, all liquids are clinopyroxene saturated, so our parameterization applies all the way to the liquidus. At high pressures ($>3$ GPa), where garnet replaces clinopyroxene on the liquidus, the limited experimental data do not show an observable drop in $(\partial F/\partial T)_P$ in the vicinity of cpx-out (i.e., when garnet is the only phase on the liquidus), although a drop in melt productivity is observed in pMELTS calculations (Figure S5). Because $F(T_{\text{cpx-out}})$ decreases with pressure below $\sim$1–1.5 GPa (based on pMELTS calculations, e.g., Figure 1 and basalt phase equilibria) [e.g., *Bartels et al.*, 1991; *Bender et al.*, 1978; *Johnston and Draper*, 1992] and above $\sim$3 GPa (e.g., Figure 4b), isobaric calculations that extend to the liquidus at these low and high pressures should be viewed with caution because above cpx-out, $(\partial F/\partial T)_P$ is not explicitly calibrated in our model. Nevertheless, we have included two approximations for melt productivity above $F(T_{\text{cpx-out}})$ in Melt-PX (see Appendix A): melt productivity can be fixed at a constant value of 0.3%/°C (a value based on limited experimental data) [*Lambart et al.*, 2009a] or simply extrapolated using the quadratic $F$ versus $T$ relationship calibrated for temperatures less than $T_{\text{cpx-out}}$. Polybaric calculations where the pyroxenite solidus is intersected at pressures somewhat above 5 GPa are potentially less problematic than isobaric calculations at these high pressures, since the relatively small degrees of melting that occur at pressures where garnet is the liquidus phase are unlikely to exhaust clinopyroxene and, with decreasing pressure, the expanding cpx phase volume is likely to bring clinopyroxene onto the liquidus.

### 4.2. Extrapolating Toward Hydrous and Carbonated Pyroxenites

The presence of $H_2O$ (and $CO_2$ at pressures above $\sim$2 GPa) significantly lowers the solidus temperature of mantle lithologies [e.g., *Asimow and Langmuir*, 2003; *Dasgupta and Hirschmann*, 2006; *Falloon and Green*, 1990; *Wyllie*, 1978]. Our parameterization is calibrated using phase relations from nominally anhydrous experiments and thus should not be used to model the partial melting of carbonated or hydrous lithologies. However, estimated bulk water contents based on measurements of quenched partial melts from nominally anhydrous piston-cylinder experiments often lie in the range of 100–500 ppm, even when efforts are made to minimize adsorbed water [e.g., *Falloon et al.*, 2001; *Hirschmann et al.*, 1998a; *Laporte et al.*, 2014; *Médard et al.*, 2008]. This suggests that the pyroxenite experiments in our data set are likely to have similar or higher bulk water contents. Moreover, this range (100–500 ppm) spans the range of estimated water contents in the mantle sources of MORBs and OIBs [*Hirschmann*, 2006, and references therein]. Thus, our parameterization can be applied to models of melt production that invoke pyroxenite melting in the context of MORB and OIB petrogenesis.

### 4.3. Extrapolating Toward Peridotite Compositions

Peridotites from xenoliths and ultramafic massifs span a wide range of compositions and modal olivine contents, from dunites with $>90\%$ olivine to pyroxene-rich lherzolites with between 40 and 50% olivine [e.g., *Marchesi et al.*, 2013; *Martin et al.*, 2015; *Peslier et al.*, 2002]. The more olivine-poor peridotites (those with lower MgO contents) overlap with the most MgO-rich pyroxenites (Figure 2 and Figure S1 in the supporting information). This observation, coupled with the absence of any coherent trend between $\Delta F$ ($= F_{\text{calculated}} - F_{\text{experimental}}$) and MgO for pyroxenites in the calibration data set (see Text S5 and

Figure S11d in the supporting information), suggests that it may be possible to extrapolate Melt-PX at least some "distance" into the peridotite field. This would be significant, since there is currently no parameterization of the peridotite solidus that formally incorporates major-element compositional effects over a range of pressures. *Hirschmann* [2000] discussed how incompatible-element contents would be expected to affect the solidus temperature of peridotite, and *Wasylenki et al.* [2003] presented a simple expression based on pMELTS calculations and experimentally bracketed solidus temperatures that defined the extent to which the peridotite solidus is depressed by increasing concentrations of $Na_2O$, $K_2O$, and $P_2O_5$ in near-solidus melts at 1 GPa. In the peridotite melting model of *Katz et al.* [2003], calculated solidus temperatures are independent of bulk composition (the model does allow for variations in modal clinopyroxene at the solidus, but these variations only affect the melt fraction at which cpx disappears from the residual assemblage).

To explore the extent to which Melt-PX can be extrapolated into the peridotite field, we selected five "peridotite" compositions with bulk MgO contents ranging from ~34 to ~42 wt %: FER-B [*Pickering-Witter and Johnston*, 2000], KR4003 [*Walter*, 1998], MM3 [*Baker and Stolper*, 1994], KLB-1 [*Hirose and Kushiro*, 1993; *Herzberg et al.*, 2000], and DMM1 [*Wasylenki et al.*, 2003]. Unfortunately, the peridotite experimental data referenced above are skewed to lower pressures (1–3 GPa), and not all compositions have been investigated in sufficient detail to tightly constrain $T_{5\%}$, $T_{cpx-out}$, and $F(T_{cpx-out})$. Nevertheless, a direct comparison between the output of Melt-PX and the experimental data suggests that our parameterization is able to predict near-solidus temperatures and disappearance temperatures of cpx for fertile peridotites to within approximately ± 30°C (Figure 5a) and ± 40°C (Figure 5b), respectively. Finally, Melt-PX substantially overestimates $F$ ($T_{cpx-out}$) for all compositions—with a suggestion that the mismatch increases with decreasing pressure (Figure 6a). This mismatch probably reflects the difference in clinopyroxene melting reaction coefficients for peridotites and pyroxenites (compare the 3 GPa melting reactions in *Walter* [1998] and *Pertermann and Hirschmann* [2003a]. Thus, although Melt-PX can be used to model the near-solidus temperatures of fertile peridotites that grade into pyroxenites (if pressures are ≤ 3 GPa), empirical parameterizations [e.g., *Katz et al.*, 2003] based on peridotite partial melting experiments should be used for modeling melt fractions of a generic fertile peridotite as a function of pressure and temperature.

## 5. Melting Behavior of Pyroxenites and Implications for Its Role in Basalt Genesis

In modeling the melting of a lithologically heterogeneous source (e.g., pyroxenite bodies embedded in a matrix of peridotite), the pyroxenite has almost universally been assumed to have a lower solidus temperature than the peridotite at all pressures [e.g., *Kogiso et al.*, 2004b; *Koornneef et al.*, 2012; *Stracke and Bourdon*, 2009; *Waters et al.*, 2011]. In part, this reflects the truism that at the pressure of melting of a natural peridotite source region, the liquidus of the partial melt will reflect the temperature of melting, but the solidus of the partial melt will be at a substantially lower temperature. Thus, the solidi of pyroxenites that have compositions that approximate those of basaltic liquids (the low MgO end of the arrays in Figures 2 and S1) are expected to be lower than the solidi of the peridotites that melted to generate those basaltic liquids. However, pyroxenites form a continuum between basaltic compositions and peridotites (Figures 2 and S1), and many of the more MgO-rich compositions may reflect the products of high-pressure crystallization within the mantle (i.e., mixtures of cumulates and intercumulus liquid) [e.g., *Downes*, 2007; *Gonzaga et al.*, 2010; *Pilet et al.*, 2011]. In this section, we use Melt-PX to explore calculated near-solidus temperatures and melt productivities up to cpx-out for the full range of observed pyroxenite compositions and to compare their melting behaviors to that of fertile peridotite (using the parameterization of *Katz et al.* [2003]). We also investigate how the predicted range in near-solidus temperatures and melt productivities might affect the amount of melting that would occur in multilithologic sources during mantle upwelling.

### 5.1. Low- and High-Solidus Lithologies

Figure 7a shows $T_{5\%}$ as a function of pressure for the 25 pyroxenites used to calibrate the parameterization (black lines; specific compositions discussed below are labeled). The thick dashed and solid red lines are the solidus and the 5% melt isopleth, respectively, for fertile peridotite [*Katz et al.*, 2003]. The thick dashed green line is an estimate of the peridotite solidus [*Hirschmann*, 2000] based on a large number of experiments on generally fertile compositions. At 1 GPa, $T_{5\%}$ calculated for the pyroxenites shown in Figure 7a spans a range of ~80°C (1169 to 1251°C); at 5 GPa, this range has increased to ~320°C (1392 to 1711°C). At 1 GPa, calculated
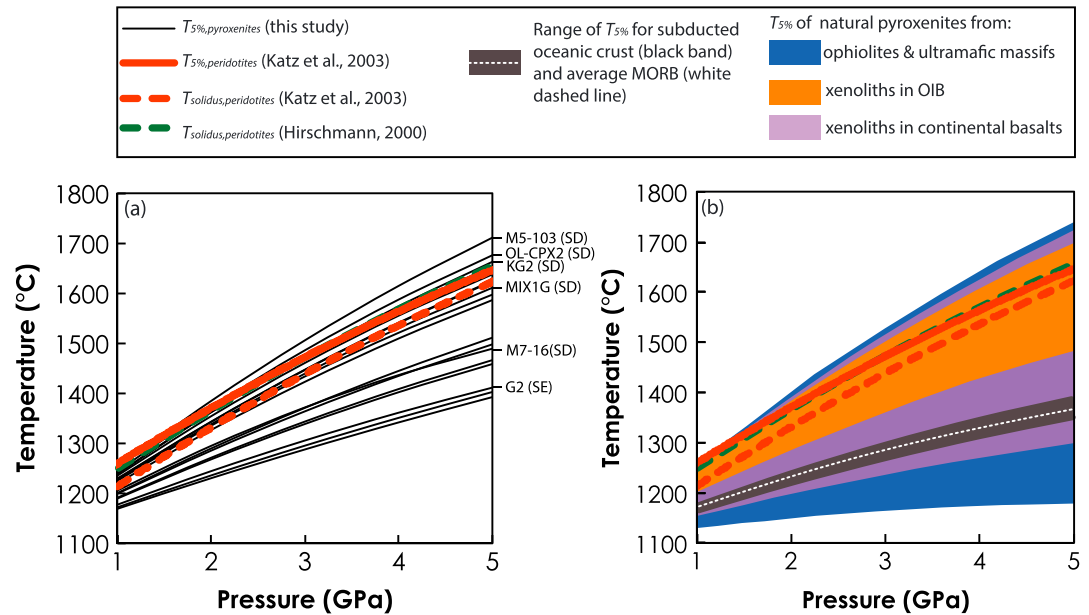
**Figure 7.** (a) Calculated $T_{5\%}$ curves (black lines) for the 18 pyroxenites used to calibrate $T_{5\%}$. Compositions G2, M7-16, MIX1G, KG2, and M5-103 discussed in the main text are labeled. (b) Colored areas are the regions defined by calculated $T_{5\%}$ values for natural pyroxenites: blue = from ophiolites and ultramafic massifs ($n = 246$), orange = as xenoliths in OIBs ($n = 29$), and purple = from gneissic and granulitic massifs and as continental xenoliths ($n = 156$). See Figure 1 in *Lambart et al.* [2009a] for references. The black band represents $T_{5\%}$ values calculated for compositions used in experimental studies on subducted oceanic crust [*Pertermann and Hirschmann*, 2003a; *Spandler et al.*, 2008; *Yaxley and Green*, 1998]. Dotted white line in the black band shows $T_{5\%}$ for average MORB [*Gale et al.*, 2013]. All calculations on pyroxenites are done using Melt-PX; the solid and dashed red lines in Figures 7a and 7b are $T_{5\%}$ and the solidus, respectively, for fertile peridotite [*Katz et al.*, 2003]; the dashed green line is the fertile peridotite solidus of *Hirschmann* [2000].

$\delta T_{5\%}$ values ($T_{5\%,pyroxenite} - T_{5\%,peridotite}$) range from approximately $-90$ to $-8°C$; the absolute magnitude of these values shows a broad positive correlation with the weight percent of normative plagioclase in each bulk composition and an inverse correlation with bulk mole percent MgO (fertile peridotite has lower normative plagioclase and higher MgO contents than all of the pyroxenites in the calibration data set). The 12 pyroxenites with the smallest absolute $\delta T_{5\%}$ values at 1 GPa are those samples that trend toward and most closely approach the cluster of peridotite compositions at the lower right end of the compositional array in Figures 2 and S1 (of these 12, 11 are SD pyroxenites; the one SE pyroxenite is Px-1). Figure 7a also shows that calculated $T_{5\%}$ values for three SD pyroxenites (M5-103, OL-CPX2, and KG2; the three most MgO-rich compositions in the calibration data set) intersect the 5% melt isopleth of fertile peridotite with increasing pressure and, by 5 GPa, plot between 15 and 63°C above it—even though their alkali contents (0.6–1.2 wt %) are substantially higher than those of fertile peridotite (e.g., 0.32 wt %, KLB-1) [*Davis et al.*, 2009].

The higher $T_{5\%}$ values of M5-103, OL-CPX2, and KG2 in comparison to that of fertile peridotite at high pressures most likely reflect several factors. (1) The expansion of the clinopyroxene phase volume with increasing pressure (i.e., $>1–2$ GPa) and reactions involving modal plagioclase to form jadeite and tschermaks components in the pyroxenes [e.g., *Kushiro and Yoder*, 1966; *Kushiro*, 1969] leads to cpx modes of pyroxenites generally becoming increasingly larger than those of peridotite as pressure increases ($D_{Na}^{cpx/liq}$ is expected to be similar for both Mg-rich pyroxenites and fertile peridotites) [*Blundy et al.*, 1995]. Higher modal clinopyroxene will lead to higher bulk partition coefficients for Na₂O between crystals and melt and therefore increased solidus temperatures. *Hirschmann* [2000] discusses this effect in the context of factors controlling near-solidus temperatures of fertile and more depleted peridotite. (2) There should be substantial differences in the compositions of high-pressure clinopyroxenes in eclogitic bulk compositions compared to those in MgO-rich pyroxenites like M5-103, OL-CPX2, and KG2—the former are extremely rich in Na and Al [e.g., *Pertermann and Hirschmann*, 2003b] and are likely to be cation deficient (i.e., contain a Ca-Eskola component) [*McCormick*, 1986; *Smyth*, 1980], while the latter (due to the much lower bulk Na and Al contents; Figures 2

and S1) are expected to be closer in composition to clinopyroxenes in peridotites (e.g., the high-pressure clinopyroxene compositions in KG1 and KG2 [*Kogiso et al.*, 1998]). These compositional differences as well as the lower Mg#s of the phases in the more eclogitic pyroxenites may contribute to explaining why pyroxenites with relatively low MgO contents have $(dT/dP)_{F=5\%}$ values lower than that of fertile peridotite (even though their modal cpx abundances are higher at high pressures). (3) As we noted above, many MgO-rich pyroxenites (nearly all of which are silica deficient; Figures 2 and S1) are thought to be cumulates produced by fractional crystallization within the lithosphere of peridotite partial melts [e.g., *Downes*, 2007; *Gonzaga et al.*, 2010]. These pyroxenites would therefore be expected to have near-solidus temperatures, at the pressures at which they formed, substantially above the temperatures at which the cumulates formed and, in turn, above the temperatures at which the peridotites partially melted. However, the presence of varying amounts of trapped melt in these cumulates [e.g., *Downes*, 2007] would tend to lower near-solidus temperatures compared to melt-free cumulates. The higher normative plagioclase abundances (i.e., $Al_2O_3$ contents) of all of the pyroxenite compositions plotted in Figure 7a relative to fertile peridotite (including M5-103, OL-CPX2, and KG2) may explain their universally negative $\delta T_{5\%}$ values at 1 GPa given the positive correlation between normative plagioclase and $\delta T_{5\%}$ values described in the previous paragraph.

Figure 7b shows fields defined by calculated $T_{5\%}$ values for pyroxenites from ophiolites and ultramafic massifs, which occur as xenoliths in ocean island basalts, and from continental settings (xenoliths in alkali basalts and kimberlites and eclogites in gneissic and granulitic massifs)—individual 5% melt isopeths calculated with Melt-PX for these 431 compositions are plotted in Figure S12. Also shown in Figure 7b are the calculated $T_{5\%}$ values for compositions thought to be representative of the subducted oceanic crust (black band) [*Pertermann and Hirschmann*, 2003a; *Spandler et al.*, 2008; *Yaxley and Green*, 1998] and for a recent compositional estimate of average MORB [*Gale et al.*, 2013]. The natural pyroxenites show a range in $T_{5\%}$ that increases from ~130°C at 1 GPa to ~560°C at 5 GPa (Figure 7b). $\delta T_{5\%}$ values at 1 GPa range from ~ 0 to −120°C (for SD pyroxenites) and −5 to −126°C (for SE pyroxenites), and, as with the calibration data set, absolute values of $\delta T_{5\%}$ at 1 GPa are positively correlated with normative plagioclase and negatively correlated with bulk MgO. Pyroxenites from ophiolites and ultramafic massifs exhibit the widest range of compositions and thus the widest range of calculated $T_{5\%}$ values (blue field in Figure 7b)—from 1129 to 1259°C at 1 GPa and 1179 to 1739°C at 5 GPa. Pyroxenites from continental settings exhibit a slightly narrower compositional range and consequently have calculated $T_{5\%}$ values at 1 and 5 GPa of 1154–1255°C and 1299–1724°C, respectively (the purple field in Figure 7b). Pyroxenites occurring as xenoliths in OIBs have more restricted compositions that yield near-solidus temperatures (orange field in Figure 7b) plotting in the upper half of the purple continental field. The $T_{5\%}$ values calculated for the average MORB composition and for three analog compositions of oceanic crust show a limited range of $T_{5\%}$ with all values near the bottom of the range of the continental pyroxenite field.

Most of the pyroxenite samples referenced in the literature come from the oceanic lithosphere [*Kogiso et al.*, 2004a] and may not be representative of pyroxenites in the source regions of MORBs or OIBs. It is important to note that the spread and differences in calculated $T_{5\%}$ values (reflecting differences in composition) between the three groups of pyroxenites may reflect a sampling bias: the biggest range corresponds to the largest group ($n = 246$ for the pyroxenites from ophiolites and ultramafic massifs)—the smallest range corresponds to the smallest group ($n = 29$ for xenoliths in OIBs). However, the diversity of lithologies in the subducted oceanic crust (e.g., silicic sediments, basalts, and gabbros) and, more importantly, the numerous interactions that can occur between these lithologies and peridotite in the convecting mantle suggest that the wide range of pyroxenite compositions that have been analyzed to date is not unexpected [*Herzberg*, 2011]. Because pyroxenite xenoliths in OIBs have likely undergone the least compositional modification during their rapid ascent to the surface [e.g., *Sun and McDonough*, 1989], they may be the most representative of pyroxenites in the convecting mantle [e.g., *Bizimis et al.*, 2007; *Keshav and Sen*, 2001]. These xenoliths have relatively high $T_{5\%}$ values (~83% are SD pyroxenites and over 30% have >30 oxide mol % MgO) suggesting that a sizable fraction of pyroxenite in OIB source regions maybe less fusible than compositions thought to be representative of the subducted oceanic crust (Figure 7b).

Assuming that $T_{5\%}$ is a reasonable approximation for near-solidus temperatures, Figure 8a illustrates, as a function of mantle potential temperature ($T_P$, i.e., the temperature of a metastable unmelted homogeneous mantle when it reaches the surface isentropically), the percentage of pyroxenite compositions reported in the
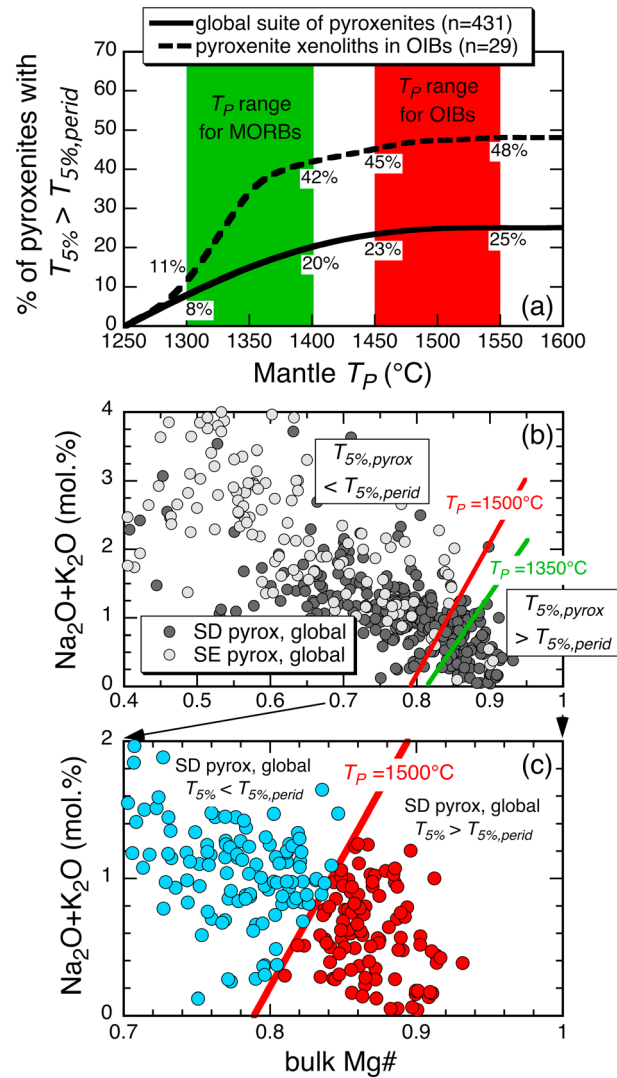
**Figure 8.** (a) Percentage of natural pyroxenite compositions [*Lambart et al.*, 2009a, and references therein] that have calculated $T_{5\%}$ (Melt-PX) $> T_{5\%,peridotite}$ [*Katz et al.*, 2003] as a function of mantle potential temperature ($T_P$) (see text for details). Green and red vertical bands denote the $T_P$ ranges for MORB and OIB, respectively, [*Courtier et al.*, 2007]; values at the boundaries of the bands denote pyroxenite percentages with $T_{5\%} > T_{5\%,peridotite}$. (b) $Na_2O + K_2O$ (oxide mole percent) versus bulk Mg# for the global suite of SD and SE pyroxenites (pyrox). Solid red and green lines separate those pyroxenites with $T_{5\%} < T_{5\%,peridotite}$ (to the left) from those with $T_{5\%} > T_{5\%,peridotite}$ (to the right) for $T_P$ values of 1500°C (red) and 1350°C (green); equations for the lines are ($Na_2O + K_2O$) $= 19.05 \cdot Mg\# - 15.03$ (red) and ($Na_2O + K_2O$) $= 15 \cdot Mg\# - 12.16$ (green). (c) Enlargement of the lower right-hand portion of Figure 8b; only SD pyroxenites are plotted and they are color coded depending on whether their $T_{5\%}$ value is $<$ or $> T_{5\%,peridotite}$ for a $T_P$ value of 1500°C.

literature that start to melt after fertile peridotite. Although it is generally assumed that near-solidus temperatures (i.e., $T_{5\%}$) for pyroxenites are below those of fertile peridotite, our modeling results show that along an adiabatic path, between 8 and 20% of pyroxenite compositions start to melt at shallower pressures than fertile peridotite for the range of estimated $T_P$ values beneath mid-ocean ridges. This proportion increases to 25% for the range of $T_P$ values estimated for oceanic islands. If we consider only pyroxenites carried by OIBs, the proportion increases to 11–42% beneath mid-ocean ridges and is up to 48% beneath oceanic islands. Figure 8b shows the global suite of SD and SE pyroxenites as a function of Mg# and molar alkali content. The red solid ($T_P = 1500°C$) and green solid ($T_P = 1350°C$) lines separate those pyroxenites with $T_{5\%} > T_{5\%,peridotite}$ from those with $T_{5\%} < T_{5\%,peridotite}$ for each respective mantle potential temperature. Note that the vast majority of pyroxenites that start to melt after fertile peridotite for either $T_P$ value are silica deficient. Figure 8c (showing only SD pyroxenites for clarity) is an enlargement of the lower right corner of Figure 8b and illustrates that the dividing line in Mg#-molar alkali space is very sharp (only the $T_P = 1500°C$ line is shown for clarity).

## 5.2. The Effect of Pyroxenite Composition on Crustal Thickness

The minor- and trace-element compositional variability of oceanic lavas suggests that strong lithological heterogeneities are present in the source regions of these magmas [e.g., *Hanson*, 1977; *Wood*, 1979; *Zindler et al.*, 1984]—an inference corroborated by the observed isotopic variations [e.g., *Allègre and Turcotte*, 1986; *White*, 1985; *Zindler and Hart*, 1986]. It is generally considered that partial melts of pyroxenite constitute a larger proportion of OIBs than they do in MORBs (and that by implication pyroxenites may comprise a larger fraction of the solid OIB source) [e.g., *Sobolev et al.*, 2007]. Iceland has long been an important locality for trying to understand the influence of pyroxenite heterogeneities on the compositions and erupted volumes of magmas. The compositional spectrum of Icelandic lavas cannot be explained using a single lithology source similar to the depleted MORB mantle [e.g., *Chauvel and Hémond*, 2000; *Elkins et al.*, 2011; *Fitton et al.*, 1997; *Kokfelt et al.*, 2006; *Koornneef et al.*,

2012; *Peate et al.*, 2010; *Shorttle and Maclennan*, 2011, 2014; *Sims et al.*, 2013; *Thirlwall et al.*, 2004; *Zindler et al.*, 1979]. Although Iceland's center is strongly affected by plume-driven upwelling, magma production in the rift zones at the coasts is thought to reflect passive plate spreading alone [*Brown and Lesher*, 2014; *Ito et al.*, 1999; *Maclennan et al.*, 2001]. In the context of passive flow, the main parameters that control the thickness of the oceanic crust generated at a mid-ocean ridge are $T_P$ (or the starting pressure of melting) [*Klein and Langmuir*, 1987, 1989], the final pressure of melting (which can depend upon a number of factors, including spreading rate) [*Shen and Forsyth*, 1995], and the composition of the source [*Hirschmann and Stolper*, 1996]. In this section, we discuss how, for a specific mantle potential temperature, the abundance and composition of pyroxenite in the source region affect total melt production and thus crustal thickness (assuming all the melt is emplaced in the crust). In the calculations below, we ignore buoyancy constraints [*Brown and Lesher*, 2014; *Shorttle et al.*, 2014]—i.e., whether the upwelling mantle would, in fact, be buoyant given the specified mass fraction of pyroxenite.

*Brown and Lesher* [2014] and *Shorttle et al.* [2014] presented calculations that simulated the process of adiabatic melting of a compositionally heterogeneous mantle with the goal of modeling the isotopic and trace-element compositions of Icelandic basalts and geophysical determinations of crustal thickness. Both studies concluded that less than 10% recycled oceanic crust in the mantle source is required to reproduce the selected compositional aspects of the lavas as well as the geophysical data. Since the two studies used different melting regimes (i.e., active versus passive upwelling) and modeled different regions of the island (center versus the coast) and thus different crustal thicknesses, it is difficult to know the extent to which the consistency in the required amount of recycled oceanic crust reflects the fact that both studies used the same pyroxenite component: G2 and its associated expression for *F* as a function of *T* and *P* [*Pertermann and Hirschmann*, 2003a]. *Shorttle et al.* [2014] also performed an adiabatic melting calculation using a less fertile pyroxenite composition (KG1) [*Kogiso et al.*, 1998] and an earlier version of the parameterization presented here to describe its melting behavior [see *Shorttle et al.*, 2014, Appendix D]. Their calculations show that the proportion of pyroxenite in the mantle source needed to reproduce the trace-element compositions of the Icelandic basalts in their data set depends on the pyroxenite composition: for G2, this proportion is 4–10%; for KG1, it is 8–15%.

To illustrate how, for the same melting model, different pyroxenite compositions affect the total amount of melt produced by a pyroxenite ± peridotite source undergoing decompression melting, we modeled the thickness of oceanic crust generated by upwelling mantle that contains between 0 and 100% of one of five different pyroxenite compositions (G2, M7-16, MIX1G, KG2, and M5-103; Table S1). We adopted the same modeling approach as that of *Shorttle et al.* [2014]. We used the equations of *Phipps Morgan* [2001] and assumed that melting and decompression occur isentropically, that thermal equilibrium is maintained between both lithologies, and that both lithologies are chemically isolated. Melts from each lithology are continuously extracted and mixed along the melting column (details concerning the calculations and equations are provided in Text S5 in the supporting information). The volume of melt produced by each lithology is controlled by several factors.

1. *Mantle potential temperature*. This governs the depth at which the adiabat crosses the solidus of the lithology with the lower melting temperature and that lithology begins to melt. Estimates for $T_P$ for Iceland range from 1430 to 1637°C (*Green et al.* [2001] and *Putirka* [2005], respectively). In the following, we used $T_P = 1450$°C for illustrative purposes. Along an adiabatic decompression path with this potential temperature, G2, M7-16, and MIX1G start to melt before the peridotite, while KG2 and M5-103 start to melt after the peridotite. As emphasized by *Phipps Morgan* [2001] and *Stolper and Asimow* [2007], when the low-solidus lithology starts to melt, heat diffuses into that lithology, enhancing the amount of melting of the low-solidus lithology and delaying the melting of the high-solidus lithology. Hence, the presence of G2, M7-16, and MIX1G in the mantle will delay the onset of peridotite melting, while melting of the peridodite will delay the onset of melting of the pyroxenites KG2 and M5-103.
2. *Final pressure of melting*. We assume that melting stops at the base of the crust [*Fram and Lesher*, 1993] (details of this calculation are discussed in Text S5 in the supporting information).
3. *Melting regime*. Numerous factors define the melting regime (e.g., active versus passive upwelling, batch versus fractional melting, melt mixing, and magma transport). Calculations presented as part of this study assume a passive flow triangular melting regime [*White et al.*, 1992] where the aggregated magma reflects mixtures of fractional melts produced everywhere in the melting zone.
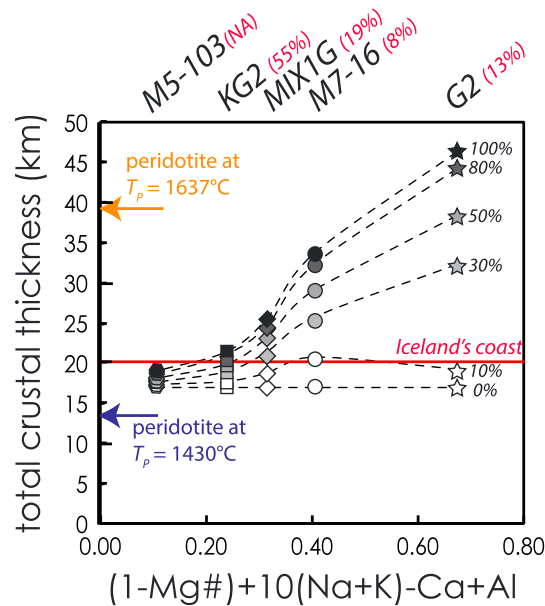
**Figure 9.** Total crustal thickness generated by adiabatic decompression of a mantle ranging from pure peridotite to 100% of each of five different pyroxenite compositions (labeled above the plot). Dashed lines connect symbols with constant percentages of pyroxenite (0, 10, 30, 50, 80, and 100%); horizontal red line denotes the mean thickness of Icelandic crust at the coast, and values in red at the top of the figure are the percentages of each pyroxenite required to generate 20 km of crust with a $T_P$ of 1450°C (melting was assumed to stop at 20 km, the base of the crust). With M5-103, the maximum oceanic crust thickness is 19 km. Arrows point to crustal thicknesses produced by a pure peridotitic mantle for potential temperatures of 1430°C and 1637°C. Pyroxenite compositions are expressed as $(1-Mg\#) + 10 \cdot (Na+K) - Ca + Al$ where Mg# is the molar ration MgO/(MgO + FeO) and Na, K, Ca, and Al are the mole fractions of $Na_2O$, $K_2O$, CaO, and $Al_2O_3$.

4.  *Melting functions.* We used the parameterization of *Katz et al.* [2003] for the peridotite component and our model, Melt-PX, for the pyroxenite component. However, since Melt-PX is only calibrated from $F = 5\%$ to the disappearance of clinopyroxene, we extrapolated the Melt-PX results to $F = 0\%$ in order to maintain consistency with the peridotite parameterization (due to the relatively high degrees of pyroxenite melting in all of the calculations, uncertainties in the 0–5% pyroxenite melting interval have little effect on the results), and we fixed the isobaric melt productivity at 0.3%/°C after cpx exhaustion (see Appendix A and Text S5 in the supporting information for more details).

Figure 9 compares oceanic crustal thicknesses generated by upwelling mantle with various proportions of G2, M7-16, MIX1G, KG2, and M5-103. The parameter $[(1 - Mg\#) + 10 \cdot (Na + K) - Ca + Al]$ is used to quantitatively illustrate the "fertility" of a given pyroxenite—$T_{5\%}$ decreases and $F$ increases with decreasing Mg# and increasing (Na + K); see equation (2); $T_{cpx\text{-}out}$ decreases and $F$ increases with increasing Al and decreasing Ca; see equation (3), and the factor of 10 before (Na + K) simply helps spread pyroxenite compositions along the *x* axis in the figure. Calculated thicknesses are compared to the crustal thickness at Iceland's coast (~20 km) [*Bjarnason and Schmeling*, 2009; *Darbyshire et al.*, 2000; *Staples et al.*, 1997] and with the thicknesses generated by a pure peridotite mantle for the entire range of potential temperatures estimated for Iceland (1430–1637°C).

These calculations show that for a source consisting solely of fertile peridotite, crustal thickness increases from 14.8 to 38.6 km as $T_P$ increases from 1430°C to 1637°C (Figure 9). At 1450°C, the crustal thickness is 16.6 km and a potential temperature of 1483°C is required to produce 20 km of crust. Hence, the observed range in crustal thicknesses from the center of Iceland (~30–40 km) to the coast (~20 km) [e.g., *Allen*, 2002; *Bjarnason and Schmeling*, 2009; *Fedorova et al.*, 2005] can be explained, to first order, by variations in $T_P$ alone. However, as mentioned above, compositions of Icelandic basalts seem to require the presence of pyroxenite in the mantle source [e.g., *Kokfelt et al.*, 2006; *Koornneef et al.*, 2012; *Sobolev et al.*, 2007] and that will also affect crustal thicknesses. The magnitude of this effect on crustal thickness strongly depends on the mass fraction and composition of the pyroxenite in the upwelling mantle. For example, a mantle source consisting of equal mass fractions of pyroxenite G2 (the most "fertile" pyroxenite used in our calculations) and peridotite produces nearly the same crustal thickness at a $T_P$ of 1450°C as does pure peridotite at a $T_P$ of 1637°C ($\Delta T = 187$°C), while a mantle source consisting of equal mass fractions of pyroxenite M5-103 (the least fertile pyroxenite) and peridotite produces the same crustal thickness (17 km) at a $T_P$ of 1450°C as does pure peridotite at a $T_P$ of 1462°C ($\Delta T = 12$°C). For a $T_P$ of 1450°C, only 8% M7-16 is required to produce the observed 20 km of crust at Iceland's coast (Figure 9); in contrast, 55% KG2 in the upwelling mantle is necessary to produce 20 km of crust. No mixtures of peridotite and pyroxenite M5-103 are capable of producing 20 km of crust given a $T_P$ of 1450°C.
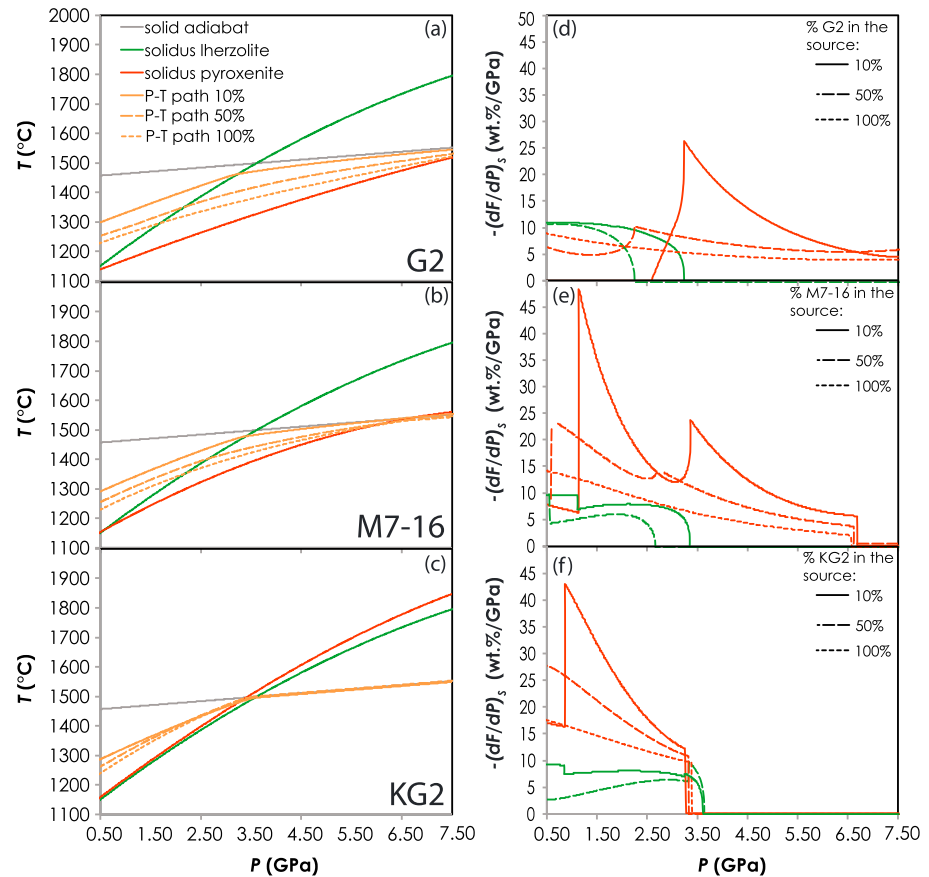
**Figure 10.** Results of model melting calculations for a mantle undergoing isentropic decompression with 10%, 50%, and 100% pyroxenite G2 (a,d), M7-16 (b,e), or KG2 (c,f) at a potential temperature of 1450°C (for the 10 and 50% cases, the pyroxenites are present as distinct lithologies). Results using pyroxenites MIX1G and M5-103 are plotted in Figures S13 and S14 in the supporting information. Figures 10a–10c show the solid adiabat (gray lines), mantle *P-T* paths (orange lines), and pyroxenite and fertile peridotite solidi (red and the green lines, respectively). Figures 10d–10f show melt productivity, $-(dF/dP)_S$, of pyroxenite (red) and fertile peridotite (green) along the corresponding adiabatic path of a column of mantle containing pyroxenite G2 (Figure 10d), M7-16 (Figure 10e), or KG2 (Figure 10f). Details concerning the calculations as well as the necessary equations are presented in Text S5 in the supporting information.

For a potential temperature of 1450°C, the extents of pyroxenite and peridotite melting for those pairs capable of producing 20 km of crust (Figure 9) are as follows: 49 and 16 wt % (55% KG2), 66 and 19 wt % (19% MIX1G), 64 and 24 wt % (13% G2), and 92 and 23 wt % (8% M7-16). The pyroxenite-derived melt contributions to the generated oceanic crust are 72% with KG2, 52% with MIX1G, 46% with G2, and 39% with M7-16. Note that even though M7-16 is less fertile than G2 (i.e., plots to the left of G2 in Figure 9), its greater extent of melting means that a smaller proportion of this pyroxenite (8%) is required to produce 20 km of crust (for a $T_P$ of 1450°C) than the more fertile pyroxenite G2 (13%). This somewhat counterintuitive result reflects the extremely shallow slope of the 5% isopleth for G2 relative to that of M7-16 (Figure 7a). Once the peridotite solidus is crossed, G2 stops melting because the adiabatic melting path is now steeper (i.e., has a higher d$T$/d$P$) than G2's solidus (Figure 10a) (see *Phipps Morgan* [2001] for further discussion). (Here and in the discussion below, we assume that the pyroxenite solidi have curvatures in *P-T* space that are similar to those of the 5% isopleths.) In contrast to G2, M7-16 and MIX1G have steeper solidi in *P-T* space and thus continue to melt, although at reduced rates (Figures 10b and S13). Thus, the steeper the pyroxenite solidus curve (in *P-T* space), the smaller the drop in pyroxenite melt productivity when the peridotite begins to melt (Figures 10d, 10e, and S13). The magnitude of this reduction in pyroxenite melting clearly depends not only on the slope the pyroxenite solidus but also on the relative proportions of peridotite and pyroxenite in the upwelling mantle—the greater the peridotite fraction, the larger the amount of latent heat that is consumed
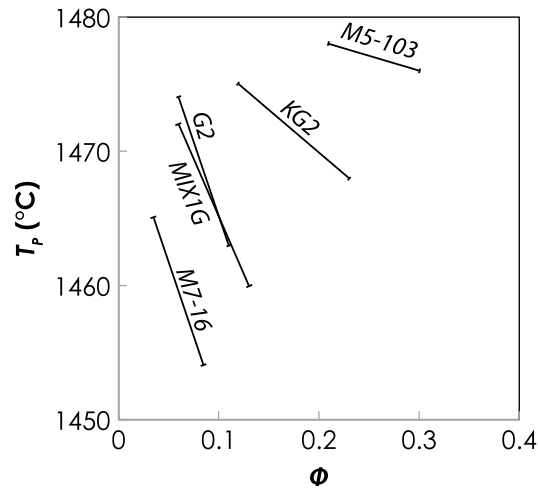
**Figure 11.** Line segments denote the range of mantle potential temperatures ($T_P$) and fractions of pyroxenite in the source ($\Phi$) required to produce a 20 km thick crust with the added constraint that $30 \pm 10\%$ of the crust be derived from pyroxenite melting [Shorttle et al., 2014]. Upwelling was assumed to be passive and melting occurred in a triangular regime. Each line segment is labeled with one of five different pyroxenites compositions used in the calculations (see Text S5 in the supporting information for details concerning the calculations).

by peridotite melting. A consequence of this thermal equilibrium between peridotite and pyroxenite is that while a 30/70 wt % mixture of G2 and peridotite produces a thicker crust than a 30/70 mixture involving M7-16 (~32 versus ~25 km), a mantle with 10% G2 and 90% peridotite produces a thinner crust (~19 km) than a mantle with 10% M7-16 and 90% peridotite (~21 km) (Figure 9). Finally, because the 5% isopeths of the pyroxenites are quadratic functions of pressure (and concave downward), the magnitude of the pyroxenite melt productivity drop is also a function of $T_P$— as $T_P$ increases, the peridotite solidus is crossed at higher pressures where the slope of pyroxenite solidus is shallower resulting in a more substantial reduction in the rate of pyroxenite melting.

Given the interplay between pyroxenite fertility, the proportion of pyroxenite in the source, and crustal thickness (Figure 9), the mass fraction of pyroxenite cannot be uniquely determined from estimates of $T_P$ and seismically constrained crustal thicknesses—at a constant $T_P$, the same crustal thickness can be generated by varying both the proportions and composition of the pyroxenite. Additional constrains such as the requirement that the upwelling mantle (peridotite + pyroxenite) be positively buoyant and estimates of the proportion of pyroxenite based on elemental and isotopic compositions of the erupted lavas may help constrain this interplay between $T_P$, mass fraction and composition of pyroxenite, and crustal thickness [e.g., Brown and Lesher, 2014; Shorttle et al., 2014; Sobolev et al., 2007]. A further constraint, that $30 \pm 10\%$ of the crust is produced by pyroxenite melting, is based on a trace-element analysis of Icelandic lavas by Shorttle et al. [2014]. (Calculating the trace-element content of the partial melts of different pyroxenites is currently beyond the scope of Melt-PX—we lack the solid phase proportions of minerals such as garnet that would be required to calculate bulk distribution coefficients.) Figure 11 shows the range of $T_P$ values and pyroxenite fractions required to produce a 20 km thick crust assuming a triangular melting regime and passive upwelling where $30 \pm 10\%$ of the crust comes from the pyroxenite. Depending on its composition, the proportion of pyroxenite required varies from 3.5–8.5% for M7-16 to 21–30% for M5-103—i.e., up to a factor of ~8.5. Consistent with the lower fertility of M5-103 relative to the other pyroxenites (Figure 9), a higher potential temperature and a larger mass fraction of M5-103 are required to reproduce the necessary crustal thickness. In principal, the trace-element content of the different pyroxenites and their partial melts coupled with the trace-element content of the primitive lavas could further winnow this suite of pyroxenite compositions. These observations emphasize that even for a relatively well-constrained system such as Iceland, where the crustal thickness is known and where the proportion of pyroxenite-derived melt to the crust has been independently estimated, it is still difficult to constrain the proportion of pyroxenite in the upwelling mantle.

## 6. Conclusions

We have developed a parameterization to calculate the near-solidus temperatures ($T_{5\%}$) and degrees of melting between 5% and the disappearance of clinopyroxene for nominally anhydrous mantle pyroxenites between pressures of 0.9 and 5 GPa—the equations have been incorporated into an Excel workbook, Melt-PX (available in the supporting information). Near-solidus temperatures are mainly controlled by the bulk alkali content and Mg#, while values of $T_{cpx-out}$ are most strongly correlated with bulk

Mg#and $Al_2O_3$ and CaO contents. When applied to our entire set of pyroxenite experimental data, the model reproduces $T_{5\%}$ and the experimental $F$ values with an average uncertainty of 30°C and 13% (absolute), respectively.

Applying our model to the global set of natural pyroxenite compositions shows that with increasing pressure, not all pyroxenites have solidus temperatures below that of fertile peridotite—along an adiabat corresponding to the $T_P$ typical of OIB mantle, about 50% of the pyroxenite xenoliths in OIBs begin to melt at a shallower depth than the peridotite begins to melt. Because all pyroxenites have near-solidus temperatures lower than those of fertile peridotites at low pressure (≤1 GPa), even "high-temperature" pyroxenites will contribute partial melt to the erupting magma if the final pressure of melting is lower than 1 GPa.

Combining our model with one for peridotite melting allows adiabatic melting calculations for a lithologically heterogeneous mantle (discrete pyroxenite blobs in a matrix of peridotite) and demonstrates that the volume of magma produced is a complex function of mantle potential temperature and mass fraction and fertility of the pyroxenite. For example, calculated crustal thicknesses using a potential temperature of 1450°C and two different mixtures of fertile peridotite and G2 (a pyroxenite commonly used in adiabatic melting calculations) vary from ~19 km (with 10% of the mantle consisting of G2) to ~32 km (with 30% G2). An interesting result of our adiabatic calculations is that if pyroxenites with shallow solidus curves in $P$-$T$ space (e.g., G2) comprise a relatively small but potentially realistic proportion (e.g., 10%) of the upwelling mantle, they stop melting once the peridotite crosses its solidus and begins to melt. Thus, they may not contribute as much melt as might be expected given their low solidus temperatures. These complexities highlight the importance of including compositional controls on near-solidus temperatures and melt fractions (between $T_{5\%}$ and $T_{cpx-out}$) when attempting to constrain potential temperatures and the proportions of pyroxenite in the mantle sources of basaltic lavas.

## Appendix A: Using Melt-PX

Here we describe the three worksheets ("Melt-PX," "decompression melting," and "range" contained in the Microsoft Excel workbook entitled Melt-PX. A copy of Melt-PX is available in the supporting information (Software).

*Melt-PX*. The first worksheet, Melt-PX, calculates the extent of isobaric batch melting of one or two pyroxenite compositions entered by the user at a user-specified pressure ($P$) and temperature ($T$). Pyroxenite bulk compositions (in oxide weight percent) and $P$ and $T$ are entered in the red-outlined cells in the dark blue region (labeled "INPUTS") in the upper left corner of the worksheet. The four figures (Mg# versus $Na_2O + K_2O$, CaO versus $Al_2O_3$, MgO versus FeO*, and MgO versus $SiO_2$, labeled "Plot 1") in the light blue region directly underneath the data entry area compare the input pyroxenite composition(s) (red square = pyroxenite A; dark blue square = pyroxenite B) with the compositions (gray diamonds) used to calibrate the model. "Plot 2" directly beneath the four composition plots compares the input pressure and temperature (black dot) with the $P$-$T$ conditions of the experimental data used to calibrate the model (region outlined in orange). Calculated values of $T_{5\%}$, $T_{cpx-out}$, and $F$, at the entered $P$ and $T$ conditions, for the two pyroxenites are reported in the green colored region labeled "OUTPUTS" to the right of the data entry area. Below OUTPUTS, "Plot 3" provides a graph of $F$ versus $T$ for the two pyroxenites (red and blue curves, respectively). The yellow and dark blue squares on each curve denote $T_{5\%}$ and $T_{cpx-out}$ for each composition at the chosen pressure. At temperatures above $T_{cpx-out}$, the dashed lines show how $F$ (for each composition) varies assuming a melt productivity of 0.3%/°C. All calculations shown on this worksheet are done in the hidden worksheets "Parameterization Pyr-A" and "Parameterization Pyr-B"; these are hidden to avoid unintentional modifications.

Three types of "alert messages" can appear depending on the inputs (i.e., oxide values entered for one or both compositions and $P$ and $T$.

1. If any of the oxides in one or both of the entered compositions fall outside of the range (minimal content used in the calibration−$1\sigma$, maximal content used in the calibration+$1\sigma$), the message "unsuitable composition" appears and symbols "!!!" appear by the oxide(s) that fall outside the range. Similarly, if the chosen $P$ does not fall within 0.9 to 5 GPa or if $T$ does not lie between 1150 and 1675°C, a message appears below the $P$ and/or $T$ input box(es) indicating that the chosen pressure and/or temperature is outside of the acceptable range.

2. If, at the chosen $P$-$T$ conditions, the calculated $F$ is < 5% or > $F(T_{cpx-out})$, a message appears in the green OUTPUTS region to remind the user that the calculation is extrapolated beyond the Melt-PX calibration. Under $P$-$T$ conditions above cpx-out, the worksheet calculates $F$ in two ways: by simple extrapolation of our model at $T > T_{cpx-out}$ and by fixing the isobaric melt productivity at 0.3%/°C above $T_{cpx-out}$, ($F'$, dashed lines in Plot 3).

3. The condition where $T_{cpx-out}, < T_{5\%}$, corresponds to the case where the subsolidus phase assemblage is clinopyroxene free. In this situation, no calculations are performed—the entered bulk composition is far outside the range of those used to parameterize the model.

4. In all cases involving extrapolation of the model, results should be used with caution.

5. Melt-PX has two compositions entered: Pyr A (red) is KG2 [*Kogiso et al.*, 1998]; Pyr B (blue) is G2 [*Pertermann and Hirschmann*, 2003a].

*Decompression melting*. This worksheet models the adiabatic decompression melting of a two-lithology mantle (pyroxenite and peridotite) in which the pyroxenite, depending on its composition, can start to melt before or after the peridotite.

Note that the pyroxenite composition must be entered under Pyr A in the worksheet Melt-PX. The peridotite is a fertile composition [see *Katz et al.*, 2003], and only its modal clinopyroxene fraction can be modified (see below).

The calculations done in this worksheet use Melt-PX for the melting functions of the pyroxenite, the parameterization of *Katz et al.* [2003] for the melting functions of the peridotite, and a modified version of the thermodynamic treatment of adiabatic fractional melting by *Phipps Morgan* [2001] (see Text S5 in the supporting information). Input parameters (to be entered into the yellow cells) are the mantle potential temperature ($T_P$), the fraction of pyroxenite in the source, and the modal clinopyroxene fraction in the subsolidus peridotite. In the cell "reduced pyroxenite melt productivity after cpx exhaustion," the user can also choose to either fix the isobaric melt productivity of the pyroxenite at 0.3 wt %/°C after cpx exhaustion (enter "1"; the default value) or to extrapolate the results of Melt-PX at $F > F(T_{cpx-out})$ (enter "0"). Default values for the heat capacities, the thermal expansivities, the densities of the solids and liquid, and the entropies of fusion (in green cells) are the same as those used in the paper (Table S2 in the supporting information). The user can change these values, but if the values are changed and the workbook is saved, the default values will be overwritten. Calculations start at 9 GPa with a pressure decrement of 10 MPa. Note that if the chosen pyroxenite starts to melt above 5 GPa, the calculations use an extrapolation of our model (see section 4.1). There are five plots on the right-hand side of the decompression melting worksheet (from left to right): (1) $T$ versus $P$ shows the adiabatic $P$-$T$ path, the solidus curves of both lithologies, and the solid adiabat; (2) $F$ versus $P$ shows the melting percentage ($F$) for each lithology; (3) $-(dF/dP)_S$ versus $P$ shows the evolution of the melt productivity at constant entropy, $-(dF/dP)_S$, for both lithologies along the decompression path; (4) oceanic crustal thickness (tc) versus $P$ shows the thickness of the oceanic crust generated along the adiabatic path; and (5) tc$^{pyr}$ versus $P$ shows the fraction of pyroxenite-derived melt in the crust.

Both Melt-PX and decompression melting are locked to avoid operating errors. The password to unlock them is pyroxenite.

*Range*. This worksheet lists all the bulk compositions that were used in our parameterization (in mole percent and in weight percent), as well as the ranges of pressure and temperature.

## References

Albarède, F., and A. Provost (1977), Petrological and geochemical mass-balance equations: An algorithm for least-square fitting and general error analysis, *Comput. Geosci.*, *3*(2), 309–326.

Allègre, C. J., and D. L. Turcotte (1986), Implications of a two-component marble-cake mantle, *Nature*, *323*(6084), 123–127.

Allen, R. M., et al. (2002), Plume-driven plumbing and crustal formation in Iceland, *J. Geophys. Res.*, *107*(B8), 2163, doi:10.1029/2001JB000584.

Arndt, N. T. (2013), Formation and evolution of the continental crust, *Geochem. Perspect.*, *2*(3), 405–533.

Asimow, P. D., and M. S. Ghiorso (1998), Algorithmic modifications extending MELTS to calculate subsolidus phase relations, *Am. Mineral.*, *83*(9-10), 1127–1132.

Asimow, P. D., and C. H. Langmuir (2003), The importance of water to oceanic mantle melting regimes, *Nature*, *421*, 815–820.

Asimow, P. D., M. M. Hirschmann, M. S. Ghiorso, M. J. O'Hara, and E. M. Stolper (1995), The effect of pressure-induced solid-solid phase transitions on decompression melting of the mantle, *Geochim. Cosmochim. Acta*, *59*(21), 4489–4506.

Asimow, P. D., M. M. Hirschmann, and E. M. Stolper (1997), An analysis of variations in isentropic melt productivity, *Philos. Trans. R. Soc. London, Ser. A*, *355*, 255–281.

Asimow, P. D., M. M. Hirschmann, and E. M. Stolper (2001), Calculation of peridotite partial melting from thermodynamic models of minerals and melts. IV. Adiabatic decompression and the composition and mean properties of mid-ocean ridge basalts, *J. Petrol.*, *42*(5), 963–998.

Baker, M. B., and E. M. Stolper (1994), Determining the composition of high-pressure mantle melts using diamond aggregates, *Geochim. Cosmochim. Acta*, *58*(13), 2811–2827.

Baker, M. B., M. M. Hirschmann, M. S. Ghiorso, and E. M. Stolper (1995), Compositions of near-solidus peridotite melts from experiments and thermodynamic calculations, *Nature*, *375*, 308–311.

Bartels, K., R. Kinzler, and T. Grove (1991), High pressure phase relations of primitive high-alumina basalts from Medicine Lake volcano, northern California, *Contrib. Mineral. Petrol.*, *108*(3), 253–270.

Beattie, P. (1993), Uranium-thorium disequilibria and partitioning on melting of garnet peridotite, *Nature*, *363*, 63–65.

Bender, J. F., F. N. Hodges, and A. E. Bence (1978), Petrogenesis of basalts from the project FAMOUS area: Experimental study from 0 to 15 kbars, *Earth Planet. Sci. Lett.*, *41*, 277–302.

Berman, R. G., and A. M. Koziol (1991), Ternary excess properties of grossular-pyrope-almandine garnet and their influence in geothermobarometry, *Am. Mineral.*, *76*(7-8), 1223–1231.

Bizimis, M., M. Griselin, J. C. Lassiter, V. J. M. Salters, and G. Sen (2007), Ancient recycled mantle lithosphere in the Hawaiian plume: Osmium–hafnium isotopic evidence from peridotite mantle xenoliths, *Earth Planet. Sci. Lett.*, *257*(1–2), 259–273.

Bjarnason, I. T., and H. Schmeling (2009), The lithosphere and asthenosphere of the Iceland hotspot from surface waves, *Geophys. J. Int.*, *178*, 394–418.

Blundy, J. D., T. J. Falloon, B. J. Wood, and J. A. Dalton (1995), Sodium partitioning between clinopyroxene and silicate melts, *J. Geophys. Res.*, *100*, 15,501–15,515, doi:10.1029/95JB00954.

Bodinier, J.-L., and M. Godard (2003), Orogenic, ophiolitic, and abyssal peridotites, in *Treatise on Geochemistry*, *The Mantle and Core*, vol. 2, edited by R. W. Carlson, pp. 103–170, Elsevier-Pergamon, Oxford, U. K.

Brown, E. L., and C. E. Lesher (2014), North Atlantic magmatism controlled by temperature, mantle composition and buoyancy, *Nat. Geosci.*, *7*(11), 820–824.

Chauvel, C., and C. Hémond (2000), Melting of a complete section of recycled oceanic crust: Trace element and Pb isotopic evidence from Iceland, *Geochem. Geophys. Geosyst.*, *1*(2), 1001, doi:10.1029/1999GC000002.

Courtier, A. M., et al. (2007), Correlation of seismic and petrologic thermometers suggests deep thermal anomalies beneath hotspots, *Earth Planet. Sci. Lett.*, *264*, 308–316.

Darbyshire, F. A., R. S. White, and K. F. Priestley (2000), Structure of the crust and uppermost mantle of Iceland from a combined seismic and gravity study, *Earth Planet. Sci. Lett.*, *181*(3), 409–428.

Dasgupta, R., and M. M. Hirschmann (2006), Melting in the Earth's deep upper mantle caused by carbon dioxide, *Nature*, *440*, 659–662.

Dasgupta, R., M. G. Jackson, and C. T. A. Lee (2010), Major element chemistry of ocean island basalts—Conditions of mantle melting and heterogeneity of mantle source, *Earth Planet. Sci. Lett.*, *289*(3–4), 377–392.

Davis, F. A., J. A. Tangeman, T. J. Tenner, and M. M. Hirschmann (2009), The composition of KLB-1 peridotite, *Am. Mineral.*, *94*, 176–180.

Day, J. M. D., D. G. Pearson, C. G. Macpherson, D. Lowry, and J.-C. Carracedo (2009), Pyroxenite-rich mantle formed by recycled oceanic lithosphere: Oxygen-osmium isotope evidence from Canary Island lavas, *Geology*, *37*(6), 555–558, doi:10.1130/G25613A.1.

Downes, H. (2007), Origin and significance of spinel and garnet pyroxenites in the shallow lithospheric mantle: Ultramafic massifs in orogenic belts in Western Europe and NW Africa, *Lithos*, *99*, 1–24.

Draper, D., and A. D. Johnston (1992), Anhydrous PT phase relations of an Aleutian high-MgO basalt: An investigation of the role of olivine-liquid reaction in the generation of arc high-alumina basalts, *Contrib. Mineral. Petrol.*, *112*(4), 501–519.

Elkins, L. J., et al. (2011), Understanding melt generation beneath the slow-spreading Kolbeinsey Ridge using $^{238}$U, $^{230}$Th, and $^{231}$Pa excesses, *Geochim. Cosmochim. Acta*, *75*(21), 6300–6329.

Elkins-Tanton, L. T. (2005), Continental magmatism caused by lithospheric delamination, *Geol. Soc. Am. Spec. Pap.*, *388*, 449–461.

Elthon, D., and C. M. Scarfe (1984), High-pressure phase equilibria of a high-magnesia basalt and the genesis of primary oceanic basalts, *Am. Mineral.*, *69*(1-2), 1–15.

Falloon, T. J., and L. V. Danyushevsky (2000), Melting of refractory mantle at 1·5, 2 and 2·5 GPa under anhydrous and H$_2$O-undersaturated conditions: Implications for the petrogenesis of high-Ca boninites and the influence of subduction components on mantle melting, *J. Petrol.*, *41*(2), 257–283.

Falloon, T. J., and D. H. Green (1990), Solidus of carbonated fertile peridotite under fluid-saturated conditions, *Geology*, *18*(3), 195–199, doi:10.1130/0091-7613(1990)018<0195:SOCFPU>2.3.CO;2.

Falloon, T. J., D. H. Green, and L. V. Danyushevsky (2001), Peridotite melting at 1 GPa: Reversal experiments on partial melt compositions produced by peridotite-basalt sandwich experiments, *J. Petrol.*, *42*, 2363–2390.

Fedorova, T., W. R. Jacoby, and H. Wallner (2005), Crust–mantle transition and Moho model for Iceland and surroundings from seismic, topography, and gravity data, *Tectonophysics*, *396*, 119–140.

Fitton, J. G., A. D. Saunders, M. J. Norry, B. S. Hardarson, and R. N. Taylor (1997), Thermal and chemical structure of the Iceland plume, *Earth Planet. Sci. Lett.*, *153*(3–4), 197–208.

Fram, M. S., and C. E. Lesher (1993), Geochemical constraints on mantle melting during creation of the North Atlantic basin, *Nature*, *363*, 712–715.

Fujii, T., and H. Bougault (1983), Melting relations of a magnesian abyssal tholeiite and the origin of MORBs, *Earth Planet. Sci. Lett.*, *62*(2), 283–295.

Gaetani, G. A., and T. L. Grove (1998), The influence of water on melting of mantle peridotite, *Contrib. Mineral. Petrol.*, *1131*, 323–346.

Gale, A., C. A. Dalton, C. H. Langmuir, Y. Su, and J.-G. Schilling (2013), The mean composition of ocean ridge basalts, *Geochem. Geophys. Geosyst.*, *14*, 489–518, doi:10.1029/2012GC004334.

Ghiorso, M. S., M. M. Hirschmann, P. W. Reiners, and V. C. Kress III (2002), The pMELTS: A revision of MELTS for improved calculation of phase relations and major element partitioning related to partial melting of the mantle to 3 GPa, *Geochem. Geophys. Geosyst.*, *3*(5), 1030, doi:10.1029/2001GC000217.

Gonzaga, R. G., D. Lowry, D. E. Jacob, A. LeRoex, D. Schulze, and M. A. Menzies (2010), Eclogites and garnet pyroxenites: Similarities and differences, *J. Volcanol. Geotherm. Res.*, *190*, 235–247.

Green, D. H., and A. E. Ringwood (1967), The genesis of basaltic magmas, *Contrib. Mineral. Petrol.*, *15*(2), 103–190.

Green, D. H., T. J. Falloon, S. M. Eggins, and G. M. Yaxley (2001), Primary magmas and mantle temperatures, *Eur. J. Mineral.*, *13*(3), 437–452.

Grove, T., E. Holbig, J. Barr, C. Till, and M. Krawczynski (2013), Melts of garnet lherzolite: Experiments, models and comparison to melts of pyroxenite and carbonated lherzolite, *Contrib. Mineral. Petrol.*, *166*(3), 887–910.

Hanson, G. N. (1977), Geochemical evolution of the suboceanic mantle, *J. Geol. Soc.*, *134*(2), 235–253.

Hauri, E. H. (1996), Major-element variability in the Hawaiian mantle plume, *Nature*, *382*, 415–419.

Hauri, E. H., and S. R. Hart (1997), Rhenium abundances and systematics in oceanic basalts, *Chem. Geol.*, *139*(1–4), 185–205.

Herzberg, C. (2006), Petrology and thermal structure of the Hawaiian plume from Mauna Kea volcano, *Nature*, *444*, 605–609.

Herzberg, C. (2011), Identification of source lithology in the Hawaiian and Canary Islands: Implications for origins, *J. Petrol.*, *52*(1), 113–146.

Herzberg, C., M. Feigenson, C. Skuba, and E. Ohtani (1988), Majorite fractionation recorded in the geochemistry of peridotites from South Africa, *Nature*, *332*(6167), 823–826.

Herzberg, C., P. Raterron, and J. Zhang (2000), New experimental observations on the anhydrous solidus for peridotite KLB-1, *Geochem. Geophys. Geosyst.*, *1*(11), 1051, doi:10.1029/2000GC000089.

Hirose, K., and I. Kushiro (1993), Partial melting of dry peridotites at high pressures: Determination of compositions of melts segregated from peridotite using aggregates of diamond, *Earth Planet. Sci. Lett.*, *114*(4), 477–489.

Hirschmann, M. M. (2000), Mantle solidus: Experimental constraints and the effects of peridotite composition, *Geochem. Geophys. Geosyst.*, *1*(10), 1042, doi:10.1029/2000GC000070.

Hirschmann, M. M. (2006), Water, melting, and the deep Earth $H_2O$ cycle, *Annu. Rev. Earth Planet. Sci.*, *34*(1), 629–653.

Hirschmann, M. M., and E. M. Stolper (1996), A possible role for garnet pyroxenite in the origin of the "garnet signature" in MORB, *Contrib. Mineral. Petrol.*, *124*(2), 185–208.

Hirschmann, M. M., M. B. Baker, and E. M. Stolper (1998a), The effect of alkalis on the silica content of mantle-derived melts, *Geochim. Cosmochim. Acta*, *62*(5), 883–902.

Hirschmann, M. M., M. S. Ghiorso, L. E. Wasylenki, P. D. Asimow, and E. M. Stolper (1998b), Calculation of peridotite partial melting from thermodynamic models of minerals and melts. I. Review of methods and comparison with experiments, *J. Petrol.*, *39*(6), 1091–1115.

Hirschmann, M. M., P. D. Asimow, M. S. Ghiorso, and E. M. Stolper (1999), Calculation of peridotite partial melting from thermodynamic models of minerals and melts. III. Controls on isobaric melt production and the effect of water on melt production, *J. Petrol.*, *40*(5), 831–851.

Hirschmann, M. M., T. Kogiso, M. B. Baker, and E. M. Stolper (2003), Alkalic magmas generated by partial melting of garnet pyroxenite, *Geology*, *31*(6), 481–484, doi:10.1130/0091-7613(2003)031<0481:AMGBPM>2.0.CO;2.

Hofmann, A. W. (2007), Sampling mantle heterogeneity through oceanic basalts: Isotopes and trace elements, in *Treatise on Geochemistry*, *The Mantle and Core*, vol. 2, edited by R. W. Carlson, H. D. Holland, and K. K. Turekian, pp. 61–101, Elsevier, Oxford, U. K.

Hofmann, A. W., and W. M. White (1982), Mantle plumes from ancient oceanic crust, *Earth Planet. Sci. Lett.*, *57*(2), 421–436.

Humphreys, E. R., and Y. Niu (2009), On the composition of ocean island basalts (OIB): The effects of lithospheric thickness variation and mantle metasomatism, *Lithos*, *112*, 118–136.

Irving, A. J. (1980), Petrology and geochemistry of composite ultramafic xenoliths in alkalic basalts and implications for magmatic processes within the mantle, *Am. J. Sci.*, *280*(A), 389–426.

Ito, G., and J. J. Mahoney (2005), Flow and melting of a heterogeneous mantle: 1. Method and importance to the geochemistry of ocean island and mid-ocean ridge basalts, *Earth Planet. Sci. Lett.*, *230*(1–2), 29–46.

Ito, G., Y. Shen, G. Hirth, and C. J. Wolfe (1999), Mantle flow, melting, and dehydration of the Iceland mantle plume, *Earth Planet. Sci. Lett.*, *165*(1), 81–96.

Iwamori, H., D. McKenzie, and E. Takahashi (1995), Melt generation by isentropic mantle upwelling, *Earth Planet. Sci. Lett.*, *134*(3–4), 253–266.

Jennings, E. S., and T. J. B. Holland (2015), A simple thermodynamic model for melting of peridotite in the system NCFMASOCr, *J. Petrol.*, *56*(5), 869–892.

Johnson, K. T. M., and I. Kushiro (1992), Segregation of high pressure partial melts from peridotite using aggregates of diamond: A new experimental approach, *Geophys. Res. Lett.*, *19*, 1703–1706, doi:10.1029/92GL01635.

Johnston, A. D., and D. S. Draper (1992), Near-liquidus phase relations of an anhydrous high-magnesia basalt from the Aleutian Islands: Implications for arc magma genesis and ascent, *J. Volcanol. Geotherm. Res.*, *52*, 27–41.

Kamber, B. S., and K. D. Collerson (2000), Role of 'hidden' deeply subducted slabs in mantle depletion, *Chem. Geol.*, *166*(3–4), 241–254.

Katz, R. F., M. Spiegelman, and C. H. Langmuir (2003), A new parameterization of hydrous mantle melting, *Geochem. Geophys. Geosyst.*, *4*(9), 1073, doi:10.1029/2002GC000433.

Kay, R. W., and P. W. Gast (1973), The rare earth content and origin of alkali-rich basalts, *J. Geol.*, *81*(6), 653–682.

Kay, R. W., and S. Mahlburg Kay (1993), Delamination and delamination magmatism, *Tectonophysics*, *219*(1–3), 177–189.

Kelemen, P. B., S. R. Hart, and S. Bernstein (1998), Silica enrichment in the continental upper mantle via melt/rock reaction, *Earth Planet. Sci. Lett.*, *164*(1–2), 387–406.

Keshav, S., and G. Sen (2001), Majoritic garnets in Hawaiian xenoliths: Preliminary results, *Geophys. Res. Lett.*, *28*, 3509–3512, doi:10.1029/2001GL012950.

Keshav, S., G. H. Gudfinnsson, G. Sen, and Y. Fei (2004), High-pressure melting experiments on garnet clinopyroxenite and the alkalic to tholeiitic transition in ocean-island basalts, *Earth Planet. Sci. Lett.*, *223*(3–4), 365–379.

Kimura, J.-I., and H. Kawabata (2015), Ocean Basalt Simulator version 1 (OBS1): Trace element mass balance in adiabatic melting of a pyroxenite-bearing peridotite, *Geochem. Geophys. Geosyst.*, *16*, 267–300, doi:10.1002/2014GC005606.

Kinzler, R. J. (1997), Melting of mantle peridotite at pressures approaching the spinel to garnet transition: Application to mid-ocean ridge basalt petrogenesis, *J. Geophys. Res.*, *102*, 853–874, doi:10.1029/96JB00988.

Kinzler, R. J., and T. L. Grove (1992a), Primary magmas of mid-ocean ridge basalts 1. Experiments and methods, *J. Geophys. Res.*, *97*, 6885–6906, doi:10.1029/91JB02840.

Kinzler, R. J., and T. L. Grove (1992b), Primary magmas of mid-ocean ridge basalts 2. Applications, *J. Geophys. Res.*, *97*, 6907–6926, doi:10.1029/91JB02841.

Klein, E. M., and C. H. Langmuir (1987), Global correlations of ocean ridge basalt chemistry with axial depth and crustal thickness, *J. Geophys. Res.*, *92*, 8089–8115, doi:10.1029/JB092iB08p08089.

Klein, E. M., and C. H. Langmuir (1989), Local versus global variations in ocean ridge basalt composition: A reply, *J. Geophys. Res.*, *94*, 4241–4252, doi:10.1029/JB094iB04p04241.

Kogiso, T., and M. M. Hirschmann (2001), Experimental study of clinopyroxenite partial melting and the origin of ultra-calcic melt inclusions, *Contrib. Mineral. Petrol.*, *142*(3), 347–360.

Kogiso, T., and M. M. Hirschmann (2006), Partial melting experiments of bimineralic eclogite and the role of recycled mafic oceanic crust in the genesis of ocean island basalts, *Earth Planet. Sci. Lett.*, *249*(3–4), 188–199.

Kogiso, T., K. Hirose, and E. Takahashi (1998), Melting experiments on homogeneous mixtures of peridotite and basalt: Application to the genesis of ocean island basalts, *Earth Planet. Sci. Lett.*, *162*(1–4), 45–61.

Kogiso, T., M. M. Hirschmann, and D. J. Frost (2003), High-pressure partial melting of garnet pyroxenite: Possible mafic lithologies in the source of ocean island basalts, *Earth Planet. Sci. Lett.*, *216*(4), 603–617.

Kogiso, T., M. M. Hirschmann, and M. Pertermann (2004a), High-pressure partial melting of mafic lithologies in the mantle, *J. Petrol.*, *45*(12), 2407–2422.

Kogiso, T., M. M. Hirschmann, and P. W. Reiners (2004b), Lenght scales of mantle heterogeneities and their relationship to ocean island basalt, *Geochim. Cosmochim. Acta*, *68*(2), 345–360.

Kokfelt, T. F., K. Hoernle, F. Hauff, J. Fiebig, R. Werner, and D. Garbe-Schönberg (2006), Combined trace element and Pb-Nd–Sr-O isotope evidence for recycled oceanic crust (upper and lower) in the Iceland mantle plume, *J. Petrol.*, *47*(9), 1705–1749.

Koornneef, J. M., A. Stracke, B. Bourdon, M. A. Meier, K. P. Jochum, B. Stoll, and K. Grönvold (2012), Melting of a two-component source beneath Iceland, *J. Petrol.*, *53*(1), 127–157.

Korenaga, J. (2013), Initiation and evolution of plate tectonics on Earth: Theories and observations, *Annu. Rev. Earth Planet. Sci.*, *41*, 117–151.

Kornprobst, J. (1970), Les péridotites et les pyroxénolites du massif ultrabasique des Beni Bouchera: Une étude expérimentale entre 1100 et 1550° C, sous 15 à 30 kilobars de pression sèche, *Contrib. Mineral. Petrol.*, *29*, 290–309.

Kornprobst, J., M. Piboule, M. Roden, and A. Tabit (1990), Corundum-bearing garnet clinopyroxenites at Beni Bousera (Morocco): Original plagioclase-rich gabbros recrystallized at depth within the mantle?, *J. Petrol.*, *31*(3), 717–745.

Kuno, H., and K.-I. Aoki (1970), Chemistry of ultramafic nodules and their bearing on the origin of basaltic magmas, *Phys. Earth Planet. Inter.*, *3*, 273–301.

Kushiro, I. (1969), Clinopyroxene solid solutions formed by reactions between diopside and plagioclase at high pressures, *Mineral. Soc. Am. Spec. Pap.*, *2*, 179–191.

Kushiro, I., and H. S. Yoder (1966), Anorthite-forsterite and anorthite-enstatite reactions and their bearing on the basalt-eclogite transformation, *J. Petrol.*, *7*, 337–362.

Lambart, S., D. Laporte, and P. Schiano (2009a), An experimental study of pyroxenite partial melts at 1 and 1.5 GPa: Implications for the major-element composition of Mid-Ocean Ridge Basalts, *Earth Planet. Sci. Lett.*, *288*(1–2), 335–347.

Lambart, S., D. Laporte, and P. Schiano (2009b), An experimental study of focused magma transport and basalt-peridotite interactions beneath mid-ocean ridges: Implications for the generation of primitive MORB compositions, *Contrib. Mineral. Petrol.*, *157*(4), 429–451.

Lambart, S., D. Laporte, A. Provost, and P. Schiano (2012), Fate of pyroxenite-derived melts in the peridotitic mantle: Thermodynamical and experimental constraints, *J. Petrol.*, *53*(3), 451–476.

Lambart, S., D. Laporte, and P. Schiano (2013), Markers of the pyroxenite contribution in the major-element compositions of oceanic basalts: Review of the experimental constraints, *Lithos*, *160–161*, 14–36.

Langmuir, C. H., E. M. Klein, and T. Plank (1992), Petrological systematics of mid-ocean ridge basalts: Constraints on melt generation beneath ocean ridges, in *Mantle Flow and Melt Generation at Mid-Ocean Ridges*, *Geophys. Monogr. Ser.*, vol. 71, pp. 183–280, AGU, Washington, D. C., doi:10.1029/GM071p0183.

Laporte, D., M. Toplis, M. Seyler, and J.-L. Devidal (2004), A new experimental technique for extracting liquids from peridotite at very low degrees of melting: Application to partial melting of depleted peridotite, *Contrib. Mineral. Petrol.*, *146*(4), 463–484.

Laporte, D., S. Lambart, P. Schiano, and L. Ottolini (2014), Experimental derivation of nepheline syenite and phonolite liquids by partial melting of upper mantle peridotites, *Earth Planet. Sci. Lett.*, *404*, 319–331.

Lassiter, J. C., E. H. Hauri, P. W. Reiners, and M. O. Garcia (2000), Generation of Hawaiian post-erosional lavas by melting of a mixed lherzolite/pyroxenite source, *Earth Planet. Sci. Lett.*, *178*(3–4), 269–284.

Lee, C. T. A. (2014), Physics and chemistry of deep continental crust recycling, in *Treatise on Geochemistry*, *The Crust*, vol. 4, 2nd ed., edited by R. L. Rudnicks, H. D. Holland, and K. K. Turekian, pp. 423–456, Elsevier, Oxford.

Le Maitre, R. W., et al. (2002), *Igneous Rocks: A Classification and Glossary of Terms*, 236 pp., Cambridge Univ. Press, Cambridge, U. K.

Longhi, J. (2002), Some phase equilibrium systematics of lherzolite melting: I, *Geochem. Geophys. Geosyst.*, *3*(3), 1020, doi:10.1029/2001GC000204.

Longhi, J. (2005), Temporal stability and pressure calibration of barium carbonate and talc/pyrex pressure media in a piston-cylinder apparatus, *Am. Mineral.*, *90*(1), 206–218.

Maaløe, S. (2004), The PT-phase relations of an MgO-rich Hawaiian tholeiite: The compositions of primary Hawaiian tholeiites, *Contrib. Mineral. Petrol.*, *148*(2), 236–246.

Maclennan, J., D. McKenzie, and K. Gronvöld (2001), Plume-driven upwelling under central Iceland, *Earth Planet. Sci. Lett.*, *194*(1–2), 67–82.

Mallik, A., and R. Dasgupta (2013), Reactive infiltration of MORB-eclogite-derived carbonated silicate melt into fertile peridotite at 3 GPa and genesis of alkalic magmas, *J. Petrol.*, *54*(11), 2267–2300.

Marchesi, C., C. J. Garrido, D. Bosch, J.-L. Bodinier, F. Gervilla, and K. Hidas (2013), Mantle refertilization by melts of crustal-derived garnet pyroxenite: Evidence from the Ronda peridotite massif, southern Spain, *Earth Planet. Sci. Lett.*, *362*, 66–75.

Martin, A. P., R. C. Price, A. F. Cooper, and C. A. McCammon (2015), Petrogenesis of the rifted southern Victoria Land lithospheric mantle, Antarctica, inferred from petrography, geochemistry, thermobarometry and oxybarometry of peridotite and pyroxenite xenoliths from the Mount Morning eruptive centre, *J. Petrol.*, *56*(1), 193–226.

McCormick, T. C. (1986), Crystal-chemical aspects of non-stoichiometric pyroxenes, *Am. Mineral.*, *71*, 1434–1440.

McDonough, W. F. (1991), Partial melting of subducted oceanic crust and isolation of its residual eclogitic lithology, *Philos. Trans. R. Soc. London*, *335*, 407–418.

McKenzie, D., and M. J. Bickle (1988), The volume and composition of melt generated by extension of the lithosphere, *J. Petrol.*, *32*(5), 1021–1091.

Médard, E., and T. Grove (2008), The effect of $H_2O$ on the olivine liquidus of basaltic melts: Experiments and thermodynamic models, *Contrib. Mineral. Petrol.*, *155*(4), 417–432.

Médard, E., C. A. McCammon, J. A. Barr, and T. L. Grove (2008), Oxygen fugacity, temperature reproducibility, and $H_2O$ contents of nominally anhydrous piston-cylinder experiments using graphite capsules, *Am. Mineral.*, *93*, 1838–1844.

Niu, Y. (2008), The origin of alkaline lavas, *Science*, *320*(5878), 883–884.

Niu, Y., and R. Batiza (1991), An empirical method for calculating melt compositions produced beneath mid-ocean ridges: Application for axis and off-axis (seamounts) melting, *J. Geophys. Res.*, *96*, 21,753–21,777, doi:10.1029/91JB01933.

O'Hara, M. J. (1972), Data reduction and projection schemes for complex compositions, in *Progress in Experimental Petrology: Third Progress Report of Research Supported by N.E.R.C. at Edinburgh and Manchester Universities,1972–1975*, edited by G. M. Biggar, pp. 103–126, The National Environment Research Council, London.

Pearson, D. G., and P. H. Nixon (1996), Diamonds in young orogenic belts: Graphitised diamonds from Beni Bousera, N. Morocco, a comparison with kimberlite-derived diamond occurrences and implications for diamond genesis and exploration, *Afr. Geosci. Rev.*, *3*, 295–316.

Pearson, D. G., G. R. Davies, P. H. Nixon, and H. J. Milledge (1989), Graphitized diamonds from a peridotite massif in Morocco and implications for anomalous diamond occurrences, *Nature*, *338*, 60–62.

Pearson, D. G., D. Canil, and S. B. Shirey (2003), Mantle samples included in volcanic rocks: Xenoliths and diamonds, in *Treatise on Geochemistry*, *The Mantle and Core*, vol. 2, edited by R. W. Carlson, H. D. Holland, and K. K. Turekian, pp. 171–275, Elsevier, Oxford, U. K.

Peate, D. W., K. Breddam, J. A. Baker, M. D. Kurz, A. K. Barker, T. Prestvik, N. Grassineau, and A. C. Skovgaard (2010), Compositional characteristics and spatial distribution of enriched Icelandic mantle components, *J. Petrol.*, *51*(7), 1447–1475.

Pertermann, M., and M. M. Hirschmann (2003a), Partial melting experiments on a MORB-like pyroxenite between 2 and 3 GPa: Constraints on the presence of pyroxenite in basalt source regions from solidus location and melting rate, *J. Geophys. Res.*, *108*(B2), 2125, doi:10.1029/2000JB000118.

Pertermann, M., and M. M. Hirschmann (2003b), Anhydrous partial melting experiments on MORB-like eclogite: Phase relations, phase compositions and mineral-melt partitioning of major elements at 2–3 GPa, *J. Petrol.*, *44*(12), 2173–2201.

Peslier, A. H., D. Francis, and J. Ludden (2002), The lithospheric mantle beneath continental margins: Melting and melt-rock reaction in Canadian Cordillera xenoliths, *J. Petrol.*, *43*(11), 2013–2047.

Phipps Morgan, J. (2001), Thermodynamics of pressure release melting of a veined plum pudding mantle, *Geochem. Geophys. Geosyst.*, *2*(4), 1001, doi:10.1029/2000GC000049.

Pickering-Witter, J., and A. D. Johnston (2000), The effects of variable bulk composition on the melting systematics of fertile peridotite assemblages, *Contrib. Mineral. Petrol.*, *140*, 190–211.

Pilet, S., J. Hernandez, P. Sylvester, and M. Poujol (2005), The metasomatic alternative for ocean island basalt chemical heterogeneity, *Earth Planet. Sci. Lett.*, *236*, 148–166.

Pilet, S., M. B. Baker, and E. M. Stolper (2008), Metasomatized lithosphere and the origin of alkaline lavas, *Science*, *320*(5878), 916–919.

Pilet, S., M. B. Baker, O. Müntener, and E. M. Stolper (2011), Monte Carlo simulations of metasomatic enrichment in the lithosphere and implications for the source of alkaline basalts, *J. Petrol.*, *52*(7–8), 1415–1442.

Prinzhofer, A., E. Lewin, and C. J. Allègre (1989), Stochastic melting of the marble cake mantle: Evidence from local study of the East Pacific rise at 12°50′N, *Earth Planet. Sci. Lett.*, *92*, 189–206.

Prytulak, J., and T. Elliott (2007), $TiO_2$ enrichment in ocean island basalts, *Earth Planet. Sci. Lett.*, *263*(3–4), 388–403.

Putirka, K. D. (2005), Mantle potential temperatures at Hawaii, Iceland, and the mid-ocean ridge system, as inferred from olivine phenocrysts: Evidence for thermally driven mantle plumes, *Geochem. Geophys. Geosyst.*, *6*, Q05L08, doi:10.1029/2005GC000915.

Putirka, K. D., H. Mikaelian, F. Ryerson, and H. Shaw (2003), New clinopyroxene-liquid thermobarometers for mafic, evolved, and volatile-bearing lava compositions, with applications to lavas from Tibet and the Snake River Plain, Idaho, *Am. Mineral.*, *88*, 1542–1554.

Rapp, R. P., N. Shimizu, M. D. Norman, and G. S. Applegate (1999), Reaction between slab-derived melts and peridotite in the mantle wedge: Experimental constraints at 3.8 GPa, *Chem. Geol.*, *160*(4), 335–356.

Robinson, J. A. C., and B. J. Wood (1998), The depth of the spinel to garnet transition at the peridotite solidus, *Earth Planet. Sci. Lett.*, *164*(1–2), 277–284.

Rosenthal, A., G. M. Yaxley, D. H. Green, J. Hermann, I. Kovacs, and C. Spandler (2014), Continuous eclogite melting and variable refertilisation in upwelling heterogeneous mantle, *Sci. Rep.*, *4*, 6099.

Rudnick, R. L., M. Barth, I. Horn, and W. F. McDonough (2000), Rutile-bearing refractory eclogites: Missing link between continents and depleted mantle, *Science*, *287*(5451), 278–281.

Salters, V. J. M., and H. J. B. Dick (2002), Mineralogy of the mid-ocean-ridge basalt source from neodymium isotopic composition of abyssal peridotites, *Nature*, *418*(6893), 68–72.

Schiano, P., J. M. Eiler, I. D. Hutcheon, and E. M. Stolper (2000), Primitive CaO-rich, silica-undersaturated melts in island arcs: Evidence for the involvement of clinopyroxene-rich lithologies in the petrogenesis of arc magmas, *Geochem. Geophys. Geosyst.*, *1*(5), 1018, doi:10.1029/1999GC000032

Shen, Y., and D. W. Forsyth (1995), Geochemical constraints on initial and final depths of melting beneath mid-ocean ridges, *J. Geophys. Res.*, *100*, 2211–2237, doi:10.1029/94JB02768.

Shorttle, O., and J. Maclennan (2011), Compositional trends of Icelandic basalts: Implications for short-length scale lithological heterogeneity in mantle plumes, *Geochem. Geophys. Geosyst.*, *12*, Q11008, doi:10.1029/2011GC003748.

Shorttle, O., J. Maclennan, and S. Lambart (2014), Quantifying lithological variability in the mantle, *Earth Planet. Sci. Lett.*, *395*, 24–40.

Sigmarsson, O., S. Carn, and J. C. Carracedo (1998), Systematics of U-series nuclides in primitive lavas from the 1730–36 eruption on Lanzarote, Canary Islands, and implications for the role of garnet pyroxenites during oceanic basalt formations, *Earth Planet. Sci. Lett.*, *162*(1–4), 137–151.

Sims, K. W. W., J. Maclennan, J. Blichert-Toft, E. M. Mervine, J. Blusztajn, and K. Grönvold (2013), Short length scale mantle heterogeneity beneath Iceland probed by glacial modulation of melting, *Earth Planet. Sci. Lett.*, *379*, 146–157.

Sleep, N. H. (1984), Tapping of magmas from ubiquitous mantle heterogeneities: An alternative to mantle plumes, *J. Geophys. Res.*, *89*, 10,029–10,041, doi:10.1029/JB089iB12p10029.

Smyth, J. R. (1980), Cation vacancies and the crystal chemistry of breakdown reactions in kimberlitic omphacites, *Am. Mineral.*, *65*, 1185–1191.

Snedecor, G. W., and W. G. Cochran (1989), *Statistical Methods*, 8th ed., 503 pp., Iowa State Univ. Press, Ames, Iowa.

Sobolev, A. V., A. W. Hofmann, S. V. Sobolev, and I. K. Nikogosian (2005), An olivine-free mantle source of Hawaiian shield basalts, *Nature*, *434*(7033), 590–597.

Sobolev, A. V., et al. (2007), The amount of recycled crust in sources of mantle-derived melts, *Science*, *316*(5823), 412–417.

Sobolev, A. V., A. W. Hofmann, G. Brügmann, and V. G. Batanova (2008), A quantitative link between recycling and osmium isotopes, *Science*, *321*(5888), 536.

Spandler, C., G. M. Yaxley, D. H. Green, and A. Rosenthal (2008), Phase relations and melting of anhydrous K-bearing eclogite from 1200 to 1600°C and 3 to 5 GPa, *J. Petrol.*, *49*(4), 771–795.

Staples, R. K., R. S. White, B. Brandsdóttir, W. Menke, P. K. H. Maguire, and J. H. McBride (1997), Färoe-Iceland Ridge Experiment 1. Crustal structure of northeastern Iceland, *J. Geophys. Res.*, *102*, 7849–7866, doi:10.1029/96JB03911.

Steebins, J. F., I. S. E. Carmichael, and L. K. Moret (1984), Heath capacities and entropies of silicate liquids and glasses, *Contrib. Mineral. Petrol.*, *86*, 131–148.

Stolper, E. M., and P. D. Asimow (2007), Insights into mantle melting from graphical analysis of one-component systems, *Am. J. Sci.*, *307*(8), 1051–1139.

Stracke, A., and B. Bourdon (2009), The importance of melt extraction for tracing mantle heterogeneity, *Geochim. Cosmochim. Acta*, *73*(1), 218–238.

Straub, S. M., A. B. LaGatta, A. L. Martin-Del Pozzo, and C. H. Langmuir (2008), Evidence from high-Ni olivines for a hybridized peridotite/pyroxenite source for orogenic andesites from the central Mexican Volcanic Belt, *Geochem. Geophys. Geosyst.*, *9*, Q03007, doi:10.1029/2007GC001583.

Sun, S.-s., and W. F. McDonough (1989), Chemical and isotopic systematics of oceanic basalts: Implications for mantle composition and processes, *Geol. Soc. London Spec. Publ.*, *42*(1), 313–345.

Sun, W., X. Ding, Y. Hu, R. E. Zartman, R. Arculus, M. B. Kamenetsky, and M. Chen (2011), The fate of subducted oceanic crust: A mineral segregation model, *Int. Geol. Rev.*, *53*(8), 879–893.

Takahashi, E., T. Shimazaki, Y. Tsuzaki, and H. Yoshida (1993), Melting study of a peridotite KLB-1 to 6.5 GPa, and the origin of basaltic magmas, *Philos. Trans. R. Soc. London*, *342*, 105–120.

Takahashi, E., K. Nakajima, and T. L. Wright (1998), Origin of the Columbia River basalts: Melting model of a heterogeneous plume head, *Earth Planet. Sci. Lett.*, *162*, 63–80.

Thirlwall, M. F., M. A. M. Gee, R. N. Taylor, and B. J. Murton (2004), Mantle components in Iceland and adjacent ridges investigated using double-spike Pb isotope ratios, *Geochim. Cosmochim. Acta*, *68*(2), 361–386.

Till, C. B., T. L. Grove, and M. J. Krawczynski (2012), A melting model for variably depleted and enriched lherzolite in the plagioclase and spinel stability fields, *J. Geophys. Res.*, *117*, B06206, doi:10.1029/2011JB009044.

Tsuruta, K., and E. Takahashi (1998), Melting study of an alkali basalt JB-1 up to 12.5 GPa: Behavior of potassium in the deep mantle, *Phys. Earth Planet. Inter.*, *107*(1–3), 119–130.

Tuff, J., E. Takahashi, and S. A. Gibson (2005), Experimental constraints on the role of garnet pyroxenite in the genesis of high-Fe mantle plume derived melts, *J. Petrol.*, *46*(10), 2023–2058.

Walter, M. J. (1998), Melting of garnet peridotite and the origin of komatiite and depleted lithosphere, *J. Petrol.*, *39*(1), 29–60.

Wasylenki, L. E., M. B. Baker, A. J. R. Kent, and E. M. Stolper (2003), Near-solidus melting of the shallow upper mantle: Partial melting experiments on depleted peridotite, *J. Petrol.*, *44*(7), 1163–1191.

Waters, C. L., K. W. W. Sims, M. R. Perfit, J. Blichert-Toft, and J. Blusztajn (2011), Perspective on the genesis of E-MORB from chemical and isotopic heterogeneity at 9–10°N East Pacific Rise, *J. Petrol.*, *52*(3), 565–602.

Whitaker, M. L., H. Nekvasil, D. H. Lindsley, and N. J. Difrancesco (2007), The role of pressure in producing compositional diversity in intraplate basaltic magmas, *J. Petrol.*, *48*(2), 365–393.

White, R. S., D. McKenzie, and K. O'Nions (1992), Oceanic crustal thickness from seismic measurements and rare earth element inversions, *J. Geophys. Res.*, *97*, 19,683–19,715, doi:10.1029/92JB01749.

White, W. M. (1985), Sources of oceanic basalts: Radiogenic isotopic evidence, *Geology*, *13*, 115–118, doi:10.1130/0091-7613(1985)13<115:SOOBRI>2.0.CO;2.

Wood, D. A. (1979), A variably veined suboceanic upper mantle-genetic significance for mid-ocean ridge basalts from geochemical evidence, *Geology*, *7*, 499–503, doi:10.1130/0091-7613(1979)7<499:AVVSUM>2.0.CO;2.

Wyllie, P. J. (1978), The effect of $H_2O$ and $CO_2$ on planetary mantles, *Geophys. Res. Lett.*, *5*, 440–442, doi:10.1029/GL005i006p00440.

Yasuda, A., T. Fujii, and K. Kurita (1994), Melting phase relations of an anhydrous mid-ocean ridge basalt from 3 to 20 GPa: Implications for the behavior of subducted oceanic crust in the mantle, *J. Geophys. Res.*, *99*, 9401–9414, doi:10.1029/93JB03205.

Yaxley, G. M. (2000), Experimental study of the phase and melting relations of homogeneous basalt + peridotite mixtures and implications for the petrogenesis of flood basalts, *Contrib. Mineral. Petrol.*, *139*(3), 326–338.

Yaxley, G. M., and D. H. Green (1998), High-pressure melting experiments on garnet clinopyroxenite and the alkalic to tholeiitic transition in ocean-island basalts, *Schweiz. Mineral. Petrogr. Mitt.*, *78*(2), 243–255.

Yaxley, G. M., and A. V. Sobolev (2007), High-pressure partial melting of gabbro and its role in the Hawaiian magma source, *Contrib. Mineral. Petrol.*, *154*, 371–383.

Zindler, A., and S. R. Hart (1986), Chemical geodynamics, *Annu. Rev. Earth Planet. Sci.*, *14*, 493–571.

Zindler, A., S. R. Hart, F. A. Frey, and S. P. Jakobsson (1979), Nd and Sr isotope ratios and rare earth element abundances in Reykjanes Peninsula basalts evidence for mantle heterogeneity beneath Iceland, *Earth Planet. Sci. Lett.*, *45*(2), 249–262.

Zindler, A., H. Staudigel, and R. Batiza (1984), Isotope and trace-element geochemistry of young Pacific seamounts: Implications for the scale of upper mantle heterogeneity, *Earth Planet. Sci. Lett.*, *70*, 175–195.